International Journal of Coal Geology 167 (2016) 119–135

Contents lists available at ScienceDirect

International Journal of Coal Geology

journal homepage: www.elsevier.com/locate/ijcoalgeo

Anisotropic swelling behaviour of coal matrix cubes exposed to water vapour: Effects of relative humidity and sample size

Jinfeng Liu *, Colin J. Peach, Christopher J. Spiers

Department of Earth Sciences, Faculty of Geosciences, Utrecht University, 3584CD Utrecht, The Netherlands

ARTICLE INFO

Article history:
Received 4 July 2016
Received in revised form 5 September 2016
Accepted 11 September 2016
Available online 24 September 2016

Keywords:
(E)CBM
3D dilatometry
Equilibrium
Swelling kinetics
Thermodynamics

ABSTRACT

Understanding the swelling behaviour of coal matrix material exposed to water vapour is of direct relevance to optimising (E)CBM recovery. However, accurate measurement of coal swelling due to water sorption presents a substantial challenge, because while measurement accuracy increases with sample size, so does equilibration time hence experiment duration. This paper reports dilatometry experiments conducted on 1 and 4 mm sized cubic samples of Brzeszcze high volatile bituminous coal. These were performed using a purpose-build, 3-dimensional (3D) dilatometer, consisting of sensitive eddy-current gap sensors. The aim was to accurately and continuously measure the volumetric response of coal matrix material during exposure to water vapour at relative humidities varied in the range of 0.1 to 95%, at a temperature of 40 °C. Our results show that the swelling strains attained at apparent equilibrium tend to be a factor of up to 1.45 higher perpendicular to bedding than in the bedding plane. In addition, the sample size strongly influences the swelling kinetics, but does not influence the equilibrium swelling strains. Moreover, the volumetric swelling strains attained at equilibrium show a near-linear dependence on relative humidity, reaching 1.37–1.43% at around 95% relative humidity. In an attempt to explain the observed behaviour, three models for swelling of unconfined coal matrix material due to water sorption were developed. These correspond to mono-layer adsorption, multiple-layer sorption, and combined mono plus multiple-layer sorption. The experimental data are equally well fitted by all three models, so that the mechanism responsible for swelling could not be uniquely identified. However, our findings do demonstrate that decreasing in-situ water activity causes significant anisotropic shrinkage of coal matrix material, pointing to injection and recirculation of dry nitrogen as a promising strategy for stimulating coal seams for CBM production and as a pre-treatment for later CO_2 injection and storage.

1. Introduction

Water present in coal seams is of profound importance in relation to coalbed methane (CBM) production, enhanced coalbed methane (ECBM) production and CO_2 storage in coal seams (e.g. Busch and Gensterblum, 2011). Water naturally present in coal must be pumped out to initiate CBM production (e.g. Moore, 2012; White et al., 2005). However, it is also frequently injected too, to stimulate reservoir permeability by means of hydrofracture (Pan and Wood, 2015; van Bergen et al., 2006). Its effects are manifold. First, the presence of water in coal reduces gas diffusivity (Pan et al., 2010). It also reduces the sorption capacity of coal to gases, such as CH_4 and CO_2, as coal has a greater affinity for adsorbing water (Busch and Gensterblum, 2011; Day et al., 2008b; Gensterblum et al., 2014; Gensterblum et al., 2013; Merkel et al., 2015). More importantly, sorption of water vapour by coal matrix material leads to several percent of swelling (Fry et al., 2009; Suuberg et al., 1993; van Bergen et al., 2009), with dry coals expanding more when exposed to a gas/water-vapour mixture than to pure CO_2 or CH_4 (Day et al., 2011). On the other hand, moist coals swell less upon exposure to CO_2 or CH_4 than dry coals (Day et al., 2011). These sorption-induced swelling effects directly influence cleat/fracture apertures and can therefore impact both coal seam permeability and gas productivity (e.g. Liu et al., 2011; van Bergen et al., 2006, 2009; White et al., 2005).

The above all point to the presence of water in coal seams having a largely negative impact on (E)CBM production and on CO_2 storage in coal seams. Conversely, removing water from a coal seam can potentially shrink the coal and increase the matrix permeability offering a stimulation technique (Fry et al., 2009; Pan, 2012). Investigation of the swelling/shrinkage behaviour of coal during exposure to water is therefore of key importance in designing and optimising ECBM production strategies.

Numerous studies have demonstrated that water molecules are primarily trapped by oxygen-bearing functional groups (mostly by carboxyl groups) present in the coal matrix, via hydrogen bonds (c.f. Allardice and Evans, 1971; Busch and Gensterblum, 2011; Kaji et al., 1986; Mu and Malhotra, 1991; Suárez et al., 1993; Yu et al., 2013). This mechanism usually traps a first layer of adsorbed water molecules with relatively

* Corresponding author.
E-mail address: j.liu1@uu.nl (J. Liu).

http://dx.doi.org/10.1016/j.coal.2016.09.011

high binding energy (c.f. Dubinin, 1980; Dubinin and Serpinsky, 1981). The thus-adsorbed water molecules then form secondary sites for attachment of additional water molecules with lower binding energy, thereby forming water clusters (c.f. Charrière and Behra, 2010; Lynch and Webster, 1982; McCutcheon et al., 2003; Nishino, 2001; Švábová et al., 2011). The total water adsorption capacity of coal is directly related to water activity or relative humidity, and is well described by the multilayer Dent model and the combined multi/single layer D'Arcy and Watt model (Charrière and Behra, 2010; McCutcheon et al., 2003; Švábová et al., 2011). Water sorption by coal is accordingly quite well understood.

However, only a few studies have focused on the swelling/shrinkage behaviour of coal in response to sorption/desorption of water. Suuberg et al. (1993) reported a 30% (maximum) volumetric shrinkage of coal upon drying, for various coal ranks ranging from bituminous to lignite. They prepared 50–100 mg coal powder samples (grain size <600 μm) from freshly collected coal, assuming them to have identical in-situ moisture contents. The samples were deposited in 3 mm inner diameter by 5 mm long tubes and settled by means of centrifuging. The sample assembly was then dried in a vacuum oven and the accompanying volumetric shrinkage was determined by measuring the length change of the sample within its tube. The precision of this method was ~2% (absolute) at best. The mass loss upon drying was simultaneously determined by weighing the samples, and showed a linear relation between shrinkage and water loss. A similar linear relation between sample volume change and water content of coals, ranging from sub-bituminous to bituminous, was also reported by Fry et al. (2009). These authors measured the swelling behaviour of coal blocks ($3 \times 1 \times 1$ cm^3) during exposure to water vapour at up to 97% RH (relative humidity), at room temperature, using both screw micrometer and optical methods. Large uncertainties in strain measurement were reported, as the smallest displacements developed were beyond the resolution of the screw micrometer. The results of more accurate (2–20%) optical methods were reported by (Day et al., 2008a). These showed maximum volumetric expansions of 0.5% for high rank coals exposed to 97% RH, increasing to 5% for lower rank coals. Pan (2012) simultaneously measured the uptake of water vapour and the associated dimensional changes of a single cylindrical sample (2.54 cm in diameter and 8.26 cm in length) of bituminous coal exposed to RH values up to 100% at room temperature, using gravimetric and screw micrometer methods. Due to the large sample size, equilibration in his experiments took around 53 days. The results showed that the sample expanded linearly with increasing sorbed water content (weight) in the first 42 days, at which point the water content of coal sample was <5% and the RH was ~97%. However, between days 42 and 53, when the sample was exposed to around 100% RH, the dimensions of the sample changed little, though the weight of the sample continued to increase as liquid water droplets formed.

Although the above authors successfully measured the rough volumetric response of coal samples to water adsorption, accurate measurement of the true equilibrium swelling/shrinkage behaviour of coal matrix material as a function of water vapour activity remains a major challenge. This is because a) the poor accuracy of the screw micrometer gauge and optical methods used requires large samples, b) large samples need long times to approach equilibrium and may fail to do so, and c) cleats present in large samples might result in reduced bulk swelling strains due to "lost swelling" at free fracture walls (Hol et al., 2014). Aside from the challenge of accurate measurements, more data are needed, than presently available, to assess the effects of swelling and shrinkage of coal due to water sorption and desorption under in-situ (E)CBM conditions, and to assess the potential for coal shrinkage and reservoir stimulation by drying.

In the present paper, we attempt to help fill these gaps in data on the volumetric response of coal to changing water activity. We report the results of continuous, 3D eddy-current dilatometry experiments performed on unconfined coal matrix cubes of high volatile bituminous coal (Brzeszcze, Poland), having edge dimensions of 1 and 4 mm,. In each experiment, the sample was equilibrated with water vapour at a constant temperature of 40 °C, using controlled RH values ranging from 0.1% to 95%. Our results show an anisotropic swelling response of the samples tied to the coal bedding. They also demonstrate a strong influence of sample size on swelling kinetics, but no influence on equilibrium strains. Our data further reveal a near-linear relation between swelling strain and relative humidity, hence water activity, which can be accurately fitted by both monolayer and multiple layer sorption-swelling models. After describing and discussing these effects, we consider the implications of our findings for ECBM production.

2. Experimental methods

2.1. Approach

In this study, we measured changes in the dimensions of 1 and 4 mm cubic samples of high volatile bituminous coal matrix material during exposure to water vapour at different relative humidities (RH). The experiments were conducted at RH values of 0.1 to 95% at a fixed temperature of 40 °C, using a specially developed, three-dimensional (3D) eddy-current dilatometer. This 3D dilatometer allowed us to measure the swelling/shrinkage response of the samples in three orthogonal directions, continuously and simultaneously, while RH was systematically varied. By correcting for effects of RH on the sensor system, equilibrium swelling/shrinkage displacements of around ±40 nm could be resolved.

2.2. Starting material and sample preparation

The experiments were performed on coal matrix samples taken from high volatile bituminous coal obtained from the Upper Silesian Basin of Poland, Brzeszcze mine (seam 364). The Brezeszcze coal has a vitrinite reflectance of 0.77 ± 0.05%, and contains 74.1% carbon, 5.3% hydrogen, 1.4% nitrogen, 0.7% sulfur and 18.5% oxygen (Hol et al., 2011). Specifically, the Brezeszcze coal contains 2.9% moisture content and 5.2% ash content. To speed up water vapour equilibration with the samples, and to investigate any effects of sample size on swelling kinetics and equilibrium swelling strain, we used two 1 mm coal cubes (Samples P1 and P2) and one 4 mm coal cube (Sample P3) for the present study.

The samples were prepared from a ~10 cm block of the Brzeszcze coal. Wafers with thickness of 1 mm and 4 mm were cut from this block, in orientations parallel to bedding. The sample cubes were then made by slicing the sheets parallel and normal to the butt cleat. This was all done by the Glass Workshop at Utrecht University, using a high-precision, digitally controlled, diamond wafering saw cooled by water. The many cubes thus prepared were subsequently dried in a vacuum oven at a temperature of 40 °C for several days to remove residual water and gas. After inspecting tens of cubes using an optical microscope, we chose two 1 mm cubes and one 4 mm cube, which were cleat-free and damage-free, for the present experiments. For each of the chosen samples, we defined the direction perpendicular to bedding plane as the *z* reference axis, with the *x* and *y* directions lying in the bedding plane in orientations perpendicular and parallel to the butt cleat (Fig. 1). It is assumed that *x*, *y*, and *z* correspond to the principal axes of sample anisotropy and therefore of swelling strain, though this cannot be guaranteed.

Immediately prior to mounting in the 3-D dilatometer, the dimensions of the 1 mm cubes were measured using a Leica DMRX optical microscope with image analysis (QWIN Pro) system, while the dimensions of the 4 mm cube were measured using a digital calliper (resolution 0.01 mm). The mass of each sample was measured using a METTLER TOLEDO MS205DU Semi-Micro Analytical Balance (resolution 0.01 mg). We took the average values of several measurements to determine the dimensions and mass of each sample (see Table 1).

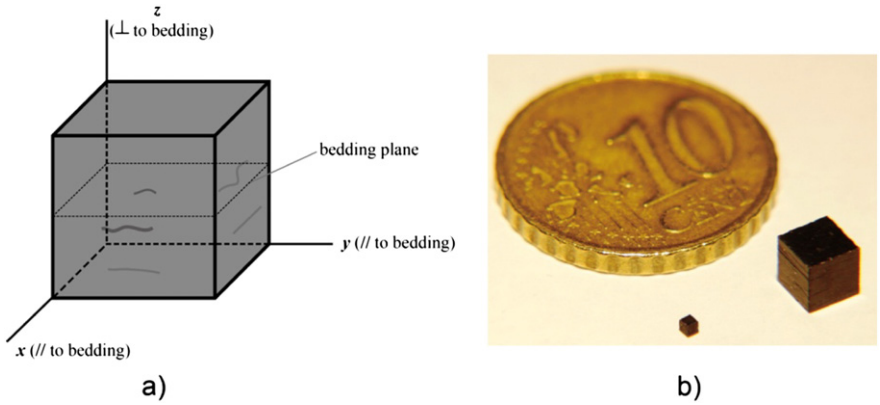

Fig. 1. a) Schematic diagram illustrating the coal matrix sample geometry used in this study. Note the *xyz* reference frame corresponding to the 3-D dilatometer measurement axes. The *x* and *y* axes lie in the bedding plane (perpendicular and parallel to the butt cleat), while *z* was defined as the direction perpendicular to bedding. b) Photograph of the 1 mm and 4 mm samples.

2.3. Apparatus

The experimental setup is shown in Fig. 2. It consists of the 3-D dilatometer (see Fig. 3) mounted in a sealed glass chamber, which is itself connected to an air circulation system controlled at fixed RH using a saturated salt solution buffer. The entire system is enclosed in a temperature controlled box.

The 3D dilatometer (Fig. 3) is composed of three independent Lion Precision type ECL202 U3B eddy current sensors (A, B, and C) mounted orthogonally in a stainless steel, multiblock frame, housing a sample stage at its centre. The sample stage contains a corner-shaped recess that supports the cubic sample on three faces in a fixed position, with the *x*, *y* and *z* sample axes aligned opposite to and coaxially with the three sensor tips (see Fig. 3). Expansion or contraction of the sample in the *x*, *y* and *z* directions is transmitted to three Aluminum eddy current targets via three, orthogonally mounted, spring cross-cantilevers that retain the sample in position. Displacement of each target, as the sample expands or contracts in the *x*, *y* or *z* direction, alters the eddy current field in the target and allows sample expansion and contraction to be measured. The full scale range of each eddy current sensor is 250 μm and the measurement resolution at fixed RH is better than ±12.5 nm.

The relative humidity employed during the experiments ranged from 0.1% to 95%. As indicated above, RH was controlled using a set of carefully selected salt solution buffers. The RH buffer system consisted of a sealed flask containing excess salt plus saturated solution, supported on a glass-fiber wool bed to ensure solid-liquid-vapour equilibration. The flask was connected to the sample chamber via a closed loop tube system incorporating a low pressure KNF gas (air) pump, used to circulate air through the flask and the glass chamber. This allowed the system to reach constant "set point" relative humidity values within 2–3 h of activation. Relative humidity within the system was measured using two SENSIRION SHT75 digital humidity sensors (accuracy ±1.8%), mounted in the inlet and outlet ports of the glass chamber containing the dilatometer. These gave consistent relative humidity values within 2% at worst. Salts used to control RH included $CuSO_4$ powders (RH = 12%), $KC_2H_3O_2$ (RH = 23%), $MgCl_2 \cdot 6H_2O$ (RH = 32%), $Mg(NO_3)_2 \cdot 6H_2O$ (RH = 49%), NaCl (RH = 75%), KCl (85%), K_2SO_4 (RH = 95%). To achieve the lowest RH value of 0.1%, phosphorus pentoxide (P_2O_5) powder was used to dry the whole buffer setup. The quality of RH control during a typical experimental run is illustrated in Fig. A1 of the Appendix A.

To maintain constant temperature of the whole setup, a ~0.42 m^3 foam-polystyrene box was constructed around it. The temperature of the air and all components inside the box, including the sample, was controlled at 39.8 °C (±0.1 °C) by means of a digital CAL 9900 PID-controller, coupled to a 500 W halogen construction lamp. Two electric fans were used to homogenize the temperature inside the box. The temperature of the sample was measured using a PT 100 element mounted on the sample stage of the dilatometer, inside the glass chamber. The controlled temperature of the whole system was measured using a PT 100 sensor located in the foam box. The quality of sample temperature control during a typical experimental run is illustrated in Fig. A2 of the Appendix A.

2.4. Dilatometer calibration and corrections

The change in each eddy current sensor signal (i.e. output voltage) with displacement of the sample target was calibrated using a specially constructed calibration jig driven by a digital micrometer screw gauge (resolution 0.1 μm). This allowed controlled translation of each target relative to the corresponding sensor tip. Calibrations were carried out at room temperature (25 °C) and room humidity (RH ≈ 50%), noting that the influence of temperature on sensitivity is known, from manufacturer's data, to be minor in the range 20–40 °C under these conditions. In each calibration run, the target was moved stepwise towards the sensor tip by rotation of the screw gauge, and the sensor output was recorded after signal stabilization. All three sensors were characterized by a closely linear relationship between voltage change and displacement over a displacement range of 250 μm, corresponding to a sensitivity of 38.8 mV/μm ($R^2 = 0.999$) for sensor A, 37.4 mV/μm ($R^2 = 0.999$) for sensor B, and 39.3 mV/μm ($R^2 = 0.999$) for sensor C. This full scale range is equivalent to a linear strain of ~25% for a 1 mm sample and ~5.1% for a 4 mm sample, with 2–3% being the maximum strains expected from previous data (Fry et al., 2009; van Bergen et al., 2009). Our

Table 1
Starting dimensions and mass of the Brzeszcze 364 coal matrix cubes used as samples in this study. The lengths L_i (where $i = x, y, z$) represent the starting dimensions in the *x*, *y* and *z* directions, as used in all strain calculations.

Sample	Initial sample mass (g)	Initial sample length L_x (μm)	Initial sample length L_y (μm)	Initial sample length L_z (μm)
P1	0.00125	941.06	1058.54	973.64
P2	0.00132	1022.51	951.61	998.5
P3	0.0848	4070	4020	4080

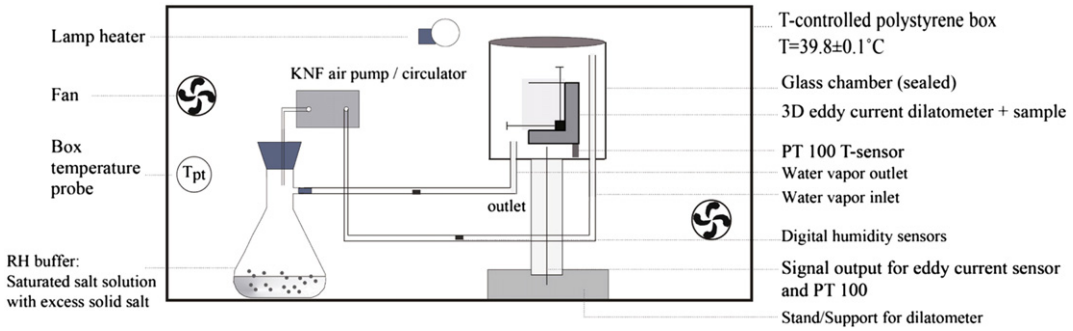

Fig. 2. Schematic diagram of the full experimental setup. The 3-D eddy current dilatometer plus sample are housed in a glass chamber. This is connected to an air flushing system incorporating a flask containing a saturated salt solution buffer for RH control. A KNF pump is used to circulate the air through the RH control system. The whole system is contained in a heated foam-polystyrene box, maintained at a controlled temperature of nominally 40 °C (specifically 39.8 ± 0.1 °C). The sample temperature and RH were measured using PT100 and digital humidity sensors, respectively.

calibration results demonstrated the resolution of the sensors in measuring sensor-target distance changes to be better than ±13 nm at room conditions.

Dummy experiments performed using 1 and 4 mm stainless steel and 1 mm quarts glass calibration cubes, instead of coal samples, showed that the eddy current sensor signals were systematically and reproducibly affected by changes in RH, presumably due to effects of water sorption on the sensor or changes in air permittivity. To calibrate this effect for all three sensors, control experiments were performed using the three dummy samples, closely replicating the experimental procedure employed in each experiment performed on coal (see details in Appendix A). This allowed correction for both transient and equilibrium effects of changes in RH on sensor signals. Equilibrium effects were corrected for using accurately fitted hyperbolic functions describing equilibrium sensor signal expressed in terms of apparent displacement (μm) versus RH. These corrections were accurate to within ±0.04 μm. Transient effects were more crudely corrected for using a linear rescaling factor (based on the ratio of corrected to raw equilibrium signals) to remove the measured effect of RH on the sensors from the apparent displacement versus time data obtained for the coal samples. Comparison of the corrections applied with the apparent displacements measured using the dummy samples, showed that the corrections for transient effects of RH changes on sensor output were accurate within ±0.15 μm.

The dummy experiments confirmed that the eddy current sensor signals were only slightly affected by changes in temperature between 20 and 40 °C. Moreover, these changes were reversible. As temperature in the present experiments was controlled within ±0.1 °C, the influence of temperature on the sensor signals could therefore be safely neglected.

2.5. Testing procedure

Four experiments were performed in total (see Table 2):

Experiment 1 (Exp1) was performed on Sample P1 and consisted of two successive RH cycling runs. Experiment 2 (Exp2) was also performed on Sample P1 but after its removed and return to the apparatus. Exp2 consisted of three successive RH cycling runs. Experiment 3 (Exp3) was performed on Sample P2 and involved two RH cycling runs. Experiment 4 (Exp4) was performed on Sample P3 and employed a single RH cycling run.

Note here that each RH cycling run performed consisted of a complete relative humidity cycle made up of 5–7 incremental steps followed by 1–4 decremental steps. All RH runs were initiated and concluded by imposing dry reference conditions upon the sample, using P_2O_5 to maintain an RH of 0.1% in the RH control system. Changes in relative humidity were achieved by manually switching the salt buffer flask. This was done within 2–3 min, during which time a disturbance in temperature of typically ~0.4 °C occurred. After each change in RH, the three eddy current sensor signals showed a transient evolution response towards an apparent equilibrium state. This was assumed to be reached when no change in signals occurred within 3–4 h. Once apparent equilibrium was reached after each RH step, we proceeded to implement the

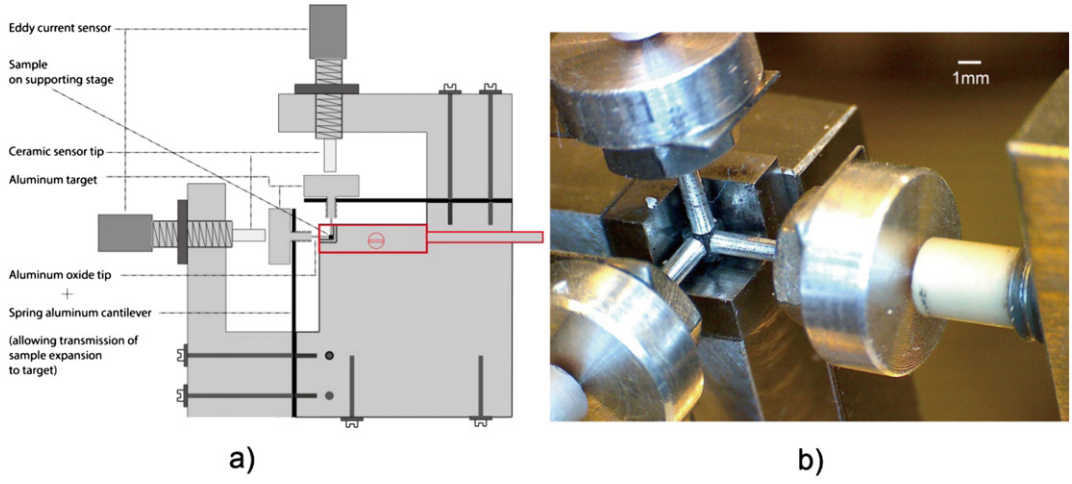

Fig. 3. The 3D dilatometer developed for this study. a) Semi-schematic diagram showing a 2D section through the sample and sample stage. Expansion or contraction of the cube-shaped sample is transmitted to three orthogonally positioned Aluminum targets via three spring cross-cantilevers that retain the sample in position. Displacement of the targets is measured using three corresponding eddy current sensors. Measurement resolution at constant RH is better than ±13 nm. b) Photograph of the 3D dilatometer with close-up of sample-stage plus 1 mm sample. Note the ceramic sensor tips.

Table 2
Summary of experiments performed. The term "run" refers to a complete relative humidity cycle containing 5–7 incremental steps in RH followed by 1–4 decremental steps in RH.

Experiment	Sample	Nominal sample size	Number of runs
Exp1	P1	1 mm	2
Exp2	P1	1 mm	3
Exp3	P2	1 mm	2
Exp4	P3	4 mm	1

next RH step. Re-equilibration of the measured sensor signals typically took ~80 h, whereas re-equilibration of the system temperature to 39.8 ± 0.1 °C took only ~1 h.

2.6. Data acquisition and processing

2.6.1. General aspects

The sample temperature and three eddy current sensors signals were logged using a National Instruments, 16-channel DAOPad-6015 A/D convertor and VI-logger data acquisition system, at a sampling rate of 0.2HZ. Relative humidity signals were digitally logged using an independent (EKH4views) system at a sampling rate of 0.1HZ, taking the average value of the relative humidity measured by the two sensors as the relative humidity during each RH step performed. Swelling displacement and strain values obtained from the eddy current sensor signals were measured as positive. We use the term "uncorrected swelling" for apparent sample strains calculated directly from the eddy current sensor signals without accounting for the effects of RH on the sensor signals. "Corrected swelling" is used to refer to the true swelling of the coal samples as calculated by applying the RH correction.

2.6.2. Processing to obtain uncorrected swelling strain versus time

The uncorrected swelling strain of our coal samples was calculated as a function of time using the expression $e_i^{uc}(t) = \frac{[V_i(t)-V_{i0}]}{S_i L_{i0}} \times 10^5$. Here $e_i^{uc}(t)$ represents uncorrected sample strain in direction i ($i = x, y, z$) at time t. The quantity $V_i(t)$ (in V) represents the sensor output signal for direction i at time t, while V_{i0} (in V) represents the signal at $t = 0$, i.e. at the initial reference condition when the sample was equilibrated at 0.1% relative humidity. In addition S_i (mV/μm) represents the sensor sensitivity in direction i, and L_{i0} (μm) is the initial dimension of the sample in this direction (before assembly).

2.6.3. Obtaining the corrected or true swelling strain at equilibrium

The time-averaged value of each sensor signal, $V_i(t)$ as obtained over the final 2 h of the *jth* RH step of each run, was taken as the mean output voltage $(\overline{V}_i)_j$ corresponding to equilibrium at RH level j. The corrected swelling strain $(e_i^{eq})_j$ expressed in % for direction i at equilibrium was computed using the expression $(e_i^{eq})_j = \frac{[(\overline{V}_i)_j - V_{i0}] \times 1000/S_i - (C_i)_j}{L_{i0}} \times 100$. Here $(C_i)_j$ represents the correction for the effect of RH on sensor for direction i at equilibrium in RH step j. As the true swelling strains $(e_i^{eq})_j$ are expected to be small, the true or corrected volumetric strain of the sample at equilibrium at RH level j is given $(e_v^{eq})_j = \sum_{i=1}^{3} (e_i^{eq})_j$. Taking the accuracy of the corrected displacement signals in the x, y and z directions at equilibrium (±0.04 μm) as a measure of uncertainty, the uncertainty of corrected volumetric strain for the 1 mm samples was within ±0.08% (absolute), while for the 4 mm sample it was within ±0.02% (absolute).

2.6.4. Obtaining corrected swelling strain versus time

The uncorrected e_i^{uc} vs. t data obtained for our coal samples could not always be accurately corrected for RH-related effects on the sensor signals, because the duration of RH steps employed in our calibration tests did not always match those used in the coal runs (see details in Appendix A.3). However, the sensor signal versus time curves obtained in the calibration tests were similar in form to the uncorrected swelling/shrinkage of coal samples versus time (see Appendix A.3). As indicated in Section 2.4, this enabled us to crudely correct the uncorrected orthogonal swelling strains $e_i^{uc}(t)$ for RH-related sensor effects, using the expression $e_i^c(t) = e_i^{uc}(t) \frac{(e_i^{eq})_j}{(e_i^{eq})_j^{uc}}$, where $e_i^c(t)$ represents the corrected swelling strain in direction i, and $(e_i^{eq})_j^{uc}$ represents the corresponding uncorrected swelling strain attained at equilibrium in RH step j. Once again, comparison of the corrections applied with the apparent displacements measured using the dummy samples, showed that the relative errors in true displacement obtained using this method were <10% (up to ±0.15 μm absolute). The largest relative errors occurred at the start of a given RH step, and decreased with time approaching to zero at equilibrium. The thus-corrected swelling data are therefore adequate for comparing swelling development with time from sample to sample, and for comparing swelling kinetics qualitatively.

3. Results

Representative data showing corrected swelling strain development in the x, y and z directions, i.e. showing $e_i^c(t)$ versus time, for individual RH cycling runs are presented in Fig. 4. The full set of (near or apparent) equilibrium swelling strains e_i^{eq} and corresponding volumetric strain e_v^{eq}, obtained for each experiment/run and each RH step (j) within each run, are presented in Table 3. Note that all swelling versus time curves presented here are plotted taking the strain and time at the onset of each experimental run as the origin.

3.1. Swelling strain development with time

With reference to Fig. 4, all experiments and all runs showed broadly similar swelling behaviour of the coal samples during exposure to water vapour. The samples expanded or shrank slowly with time, in the x, y and z directions, after each RH increment or decrement, gradually approaching an asymptotic swelling strain value in each direction. The magnitude of the (apparent) equilibrium strain systematically increased with increasing RH, and decreased with decreasing RH, in respectively the upward and downward stages of each RH cycling run. The equilibrium swelling strains e_i^{eq} attained at specific RH values were also similar in all experiments and runs, though the strains in the z direction were usually the highest, demonstrating significant swelling anisotropy especially at RH values above 12–48%. Changes in equilibrium strain per RH step were almost always largest in the z direction, with those in the x and y directions being up to 25% lower, though the 4 mm sample (Fig. 4d) was more isotropic in its behaviour than the 1 mm samples (Fig. 4a–c). The maximum total axial swelling strain occurred at relative humidities of 92.2–95.6% in all runs, reaching values of 0.51–0.55% normal to bedding plane (z direction) and 0.4–0.48% parallel to bedding plane (x and y directions).

Overall, the swelling strains developed during RH cycling were closely recoverable (Fig. 4). However, different levels of hysteresis were observed between experiments. Apparent equilibration was also faster for adsorption than for desorption, following similar changes in RH. In addition, equilibration times clearly depended on sample size. For example, the total time elapsed per run in Exp1-SampleP1-Run2 and Exp2_SampleP1_Run1 (1 mm, 7 RH steps) was 490–520 h, compared with a run duration for Exp4_SampleP3_Run1 (4 mm, 7 RH steps) of approximately 2700 h (Fig. 4b–d). Focusing on individual RH steps, in the experiments on the 1 mm samples, the time taken to approach apparent equilibrium after each RH increment lay in the range 30–150 h, depending on the magnitude of the RH change, and was about the same per RH step in all runs. By contrast, the times taken to reach apparent equilibrium per RH step in the run performed on Sample P3 (4 mm, in Exp4_SampleP3) fell in the range 100–1250 h. In particular, when the relative humidity decreased from about 49% to 0.1%, apparent equilibration for Sample P1 (1 mm) took 95–120 h, while that

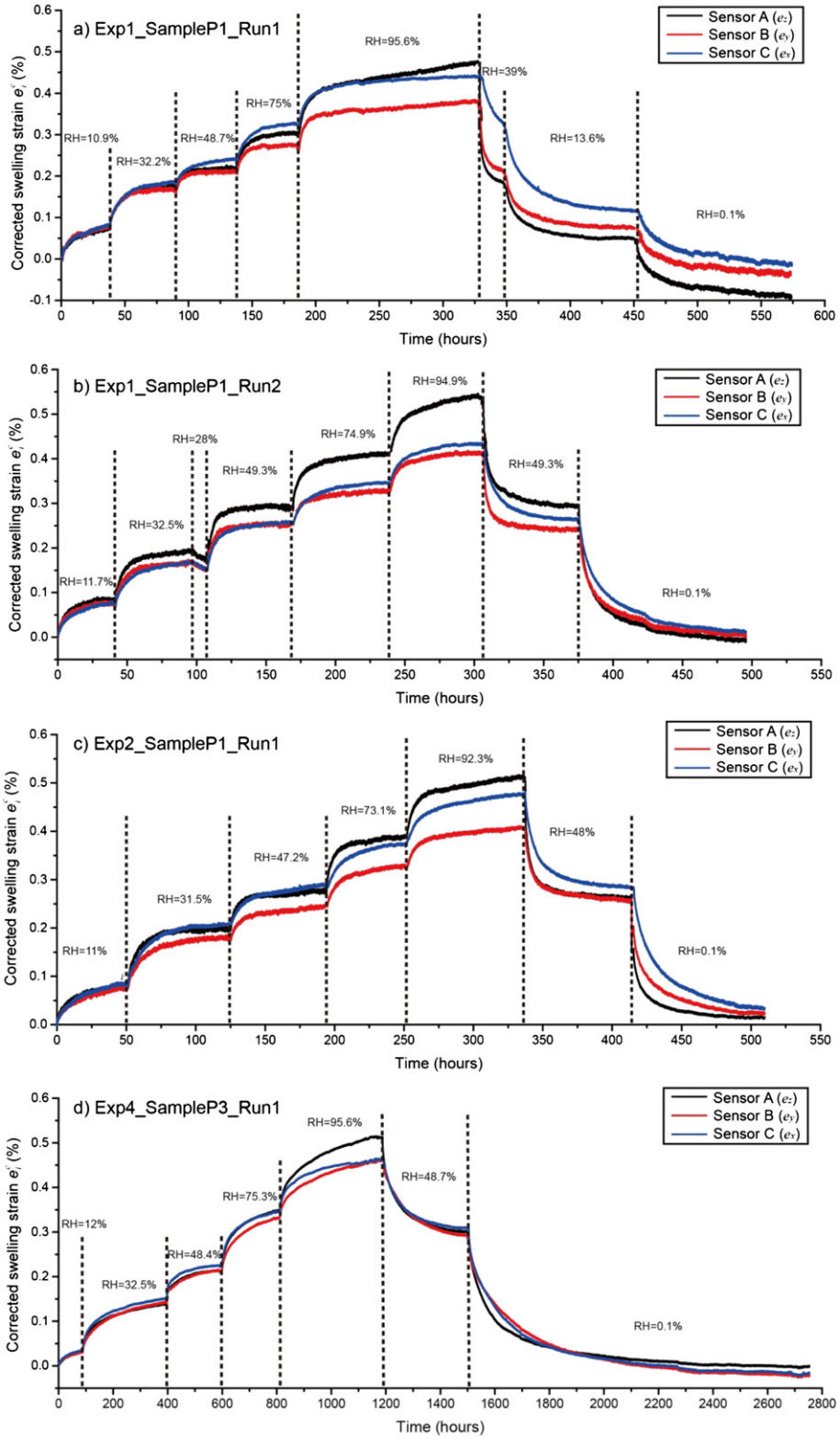

Fig. 4. a) to d). Representative curves showing corrected swelling strain e_i^c(%) versus time data as obtained in the present experiments.

for Sample P3 took about 1250 h. Equilibration times were thus much longer for the 4 mm than the 1 mm samples.

3.2. Equilibrium swelling strain versus relative humidity

As described above and visible from Table 3, the corrected swelling strains e_i^{eq} $(i = x, y, z)$ attained at (apparent) equilibrium in all experiments were similar, for similar values of imposed relative humidity. Moreover, the equilibrium strains e_i^{eq} showed a systematic direct dependence on RH, increasing with increasing RH and decreasing with decreasing RH (Fig. 4; Table 3). This dependence is illustrated for Exp1_SampleP1, Exp2_SampleP1 and Exp4_SampleP3 in Fig. 5. The data show a near-linear relation for each run, with similar sensitivities of strain to RH being obtained in all cases (around 5.4×10^{-3}% strain

Table 3
The full set of (near/apparent) equilibrium swelling strain (e_i^{eq}) data and corresponding volumetric strain (e_v^{eq}) data obtained for each experiment/run and each RH step within each run.

Sample/exp.	Run 1					Run 2 (where performed)					Run 3 (where performed)				
	RH (%)	e_z (%)	e_y (%)	e_x (%)	e_v (%)	RH (%)	e_z (%)	e_y (%)	e_x (%)	e_v (%)	RH (%)	e_z (%)	e_y (%)	e_x (%)	e_v (%)
P1/Exp1	0.1	0.000	0.000	0.000	0.000	0.1	0.000	0.000	0.000	0.000					
	10.8	0.073	0.078	0.081	0.232	11.7	0.083	0.077	0.077	0.237					
	32.5	0.174	0.166	0.185	0.525	32.5	0.189	0.165	0.165	0.519					
	49.3	0.219	0.212	0.241	0.672	49.3	0.293	0.254	0.255	0.802					
	75.3	0.304	0.271	0.324	0.898	74.6	0.411	0.328	0.345	1.084					
	95.6	0.473	0.379	0.440	1.292	94.9	0.542	0.414	0.434	1.390					
	12.9	0.035	0.076	0.119	0.229	49.3	0.295	0.241	0.264	0.800					
	0.1	−0.079	−0.021	0.015	−0.085	0.1	−0.004	0.001	0.011	0.008					
P1/Exp2	0.1	0.000	0.000	0.000	0.000	0.1	0.000	0.000	0.000	0.000	0.1	0.000	0.000	0.000	0.000
	11.0	0.080	0.075	0.084	0.239	10.0	0.066	0.059	0.063	0.188	13.3	0.081	0.075	0.075	0.232
	31.5	0.196	0.180	0.206	0.582	31.0	0.202	0.176	0.203	0.580	31.3	0.188	0.165	0.178	0.531
	47.2	0.276	0.243	0.289	0.808	48.1	0.285	0.242	0.286	0.813	47.6	0.269	0.222	0.238	0.729
	73.1	0.389	0.328	0.373	1.090	71.9	0.390	0.312	0.360	1.063	72.3	0.385	0.315	0.333	1.034
	92.3	0.512	0.408	0.476	1.395	92.6	0.548	0.403	0.465	1.415	92.2	0.523	0.412	0.456	1.391
	48.0	0.262	0.256	0.284	0.801	49.5	0.279	0.244	0.253	0.776	49.0	0.278	0.261	0.279	0.818
	0.1	−0.014	0.023	0.033	0.042	11.7	0.055	0.071	0.071	0.196	0.1	−0.036	−0.003	−0.020	−0.059
						0.1	−0.043	−0.013	−0.016	−0.072					
P2/Exp3	0.1	0.000	0.000	0.000	0.000	0.1	0.000	0.000	0.000	0.000					
	11.3	0.062	0.054	0.056	0.172	12.9	0.113	0.074	0.106	0.292					
	23.2	0.136	0.105	0.127	0.368	33.4	0.203	0.149	0.217	0.568					
	33.4	0.191	0.149	0.178	0.519	48.2	0.282	0.185	0.282	0.749					
	50.5	0.282	0.207	0.256	0.745	76.6	0.446	0.274	0.416	1.136					
	76.1	0.434	0.276	0.376	1.085	95.8	0.579	0.322	0.501	1.403					
	83.2	0.489	0.307	0.405	1.200	49.6	0.324	0.215	0.332	0.872					
	95.7	0.591	0.352	0.471	1.415	0.1	0.015	0.018	0.043	0.077					
	83.0	0.518	0.324	0.409	1.252										
	49.1	0.343	0.233	0.269	0.844										
	33.5	0.267	0.202	0.217	0.686										
	23.9	0.187	0.141	0.135	0.463										
	12.9	0.126	0.097	0.085	0.308										
	0.1	−0.011	−0.001	−0.052	−0.065										
P3/Exp4	0.1	0.000	0.000	0.000	0.000										
	12.0	0.031	0.031	0.035	0.097										
	32.5	0.139	0.143	0.151	0.433										
	48.4	0.213	0.213	0.223	0.648										
	75.3	0.349	0.332	0.345	1.026										
	95.6	0.516	0.459	0.460	1.435										
	48.7	0.301	0.293	0.310	0.903										
	0.1	−0.001	−0.022	−0.016	−0.039										

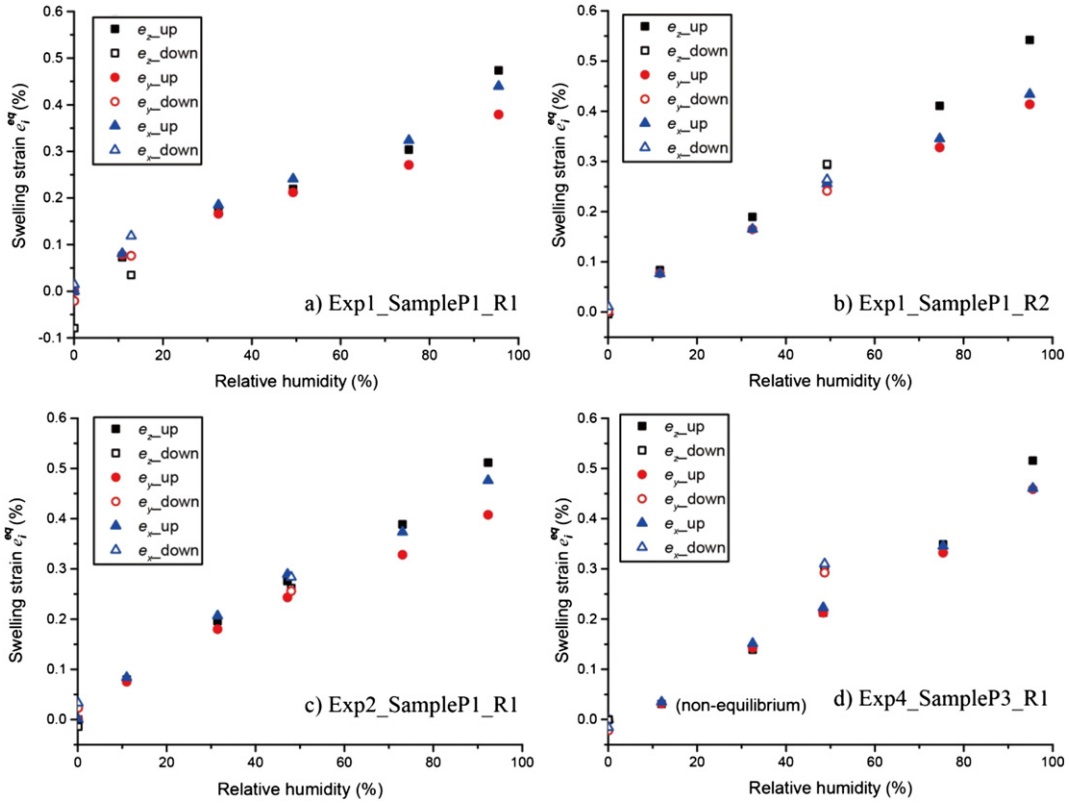

Fig. 5. Representative data showing the swelling strains e_i^{eq} (%) attained at (apparent) equilibrium, in the *x*, *y* and *z* directions of our coal samples, as a function of relative humidity (%). "Up" refers to upward RH stepping (RH increments), while "down" refers to downward RH stepping (RH decrements).

per % RH in *z* direction versus around 4×10^{-3}% strain per % RH in directions of *x* and *y*). In detail, Exp1_Run1 (Fig. 5a) showed a slightly lower sensitivity of equilibrium swelling strains e_z^{eq} to RH (4.6×10^{-3}% strain per % RH) compared with the other experiments.

Minor hysteresis was observed in the equilibrium strain vs. RH data obtained in upward vs. downward RH steps for Exp1_SampleP1_Run1 (Fig. 5a). However, this disappeared in Run2 on the same sample (Fig. 5b). Exp2_SampeP1_Run1 (Fig. 5c) also showed closely reversible behaviour in upward vs. downward RH steps. By contrast, Exp4_SampleP3_Run1 (see Fig. 5d) showed clear hysteresis. In this case, the equilibrium swelling strains obtained in all three directions at 49% RH were 30% higher in the downward RH steps than in the upward steps, though the sample finally shrank back to or even slightly beyond its initial dimensions when the relative humidity was returned to 0.1%.

Interestingly, in Exp4 (Sample P3, 4 mm), the equilibrium swelling strains attained at 12% relative humidity were $e_z = 0.031\%$, $e_y = 0.031\%$ and $e_x = 0.035\%$, which are all about one third of the values attained in Exp1 and Exp2 for the 1 mm sample P1 at 12% relative humidity. At the same time, we note that the time allowed for equilibration at 12% relative humidity in Exp4 was much shorter than allowed for the other RH values used in Exp4 (see Fig. 4d), suggesting that equilibrium was not yet attained at 12% relative humidity in Exp4.

3.3. Equilibrium volumetric swelling strain versus relative humidity

The true volumetric swelling strains (e_v^{eq}) obtained at apparent equilibrium, for all samples and all experimental runs are plotted in Fig. 6 as a function of relative humidity. All runs showed similar volumetric swelling strains (e_v^{eq}) at a given RH, except for Exp1_SampleP1_R1 which showed slightly lower swelling strain and about 0.1% of excess shrinkage at the end of the run. The volumetric swelling strain exhibited by all samples in all runs is seen to be nearly linearly proportional to relative humidity, reaching values of 1.37–1.43% at around 95% relative humidity (see Fig. 6e). The sensitivity/slop of e_v^{eq} vs. RH data yielded 0.0141–0.0149 ($R^2 = 0.99$). Additionally, all experiments illustrate that the swelling/shrinkage deformation of our samples upon adsorption/desorption of water vapour is recoverable, though with different amounts of (minor) hysteresis. Exp4_SampleP3_R1 showed the most hysteresis, while Exp1 and Exp2 performed on sample P1 showed nearly fully reversible volumetric swelling.

3.4. Optical observations on samples before and after testing

Before and after each experiment, the samples tested (P1, P2, P3) were examined in reflected light using a Leica DMRX optical microscope. At the objective magnification (10×) and scale of optical resolution used (~5 μm), no changes in sample appearance and no evidence of damage were observed after the experiments. Representative micrographs of Sample P1 taken before and after Exp2 are presented in Fig. 7.

4. Discussion

We have measured the 3-D strain response of 1 and 4 mm, cleat-free, coal matrix cubes to changes in RH, hence water vapour activity, under unconfined conditions at 40 °C and at one atmosphere total pressure. Our experimental results show a) anisotropic swelling/shrinkage behaviour with the largest strains occurring mainly normal to bedding, b) recoverability of swelling strain but with hysteresis and minor permanent strain in some cases (e.g. Exp3_SampleP2_R2), c) a strong effect of sample size on equilibration time, but no effect on swelling strain attained at apparent equilibration, and d) a near-linear relation between (apparent) equilibrium swelling strains and relative humidity.

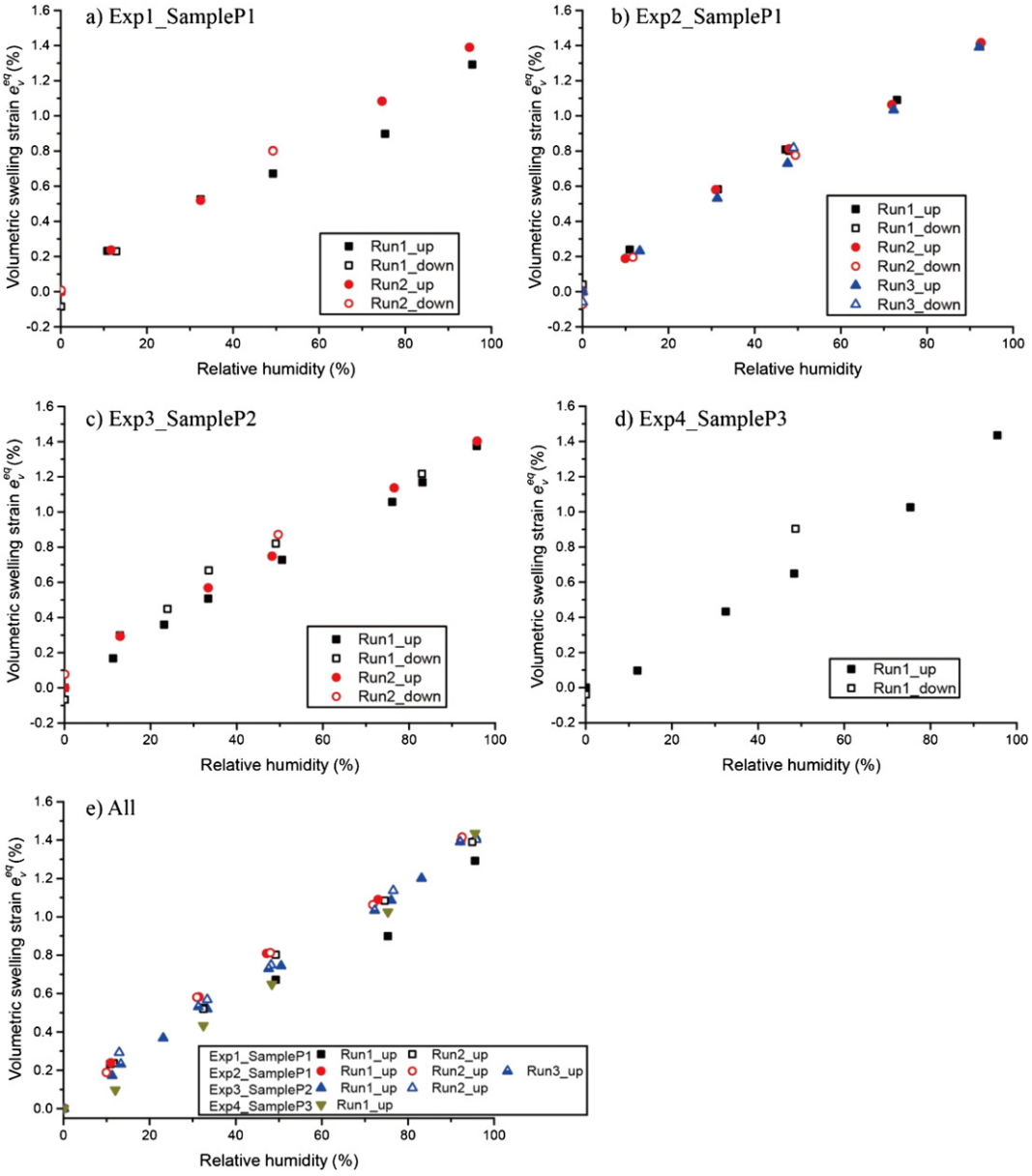

Fig. 6. True volumetric swelling strain e_v^{eq} (%) attained at (apparent) equilibrium for all samples, plotted as a function of relative humidity (%). a)–d) indicate Exp1–4 respectively, while e) shows all data combined for upward stepping RH. The RH down-stepping data are relative few and for this reason are not plotted separately here.

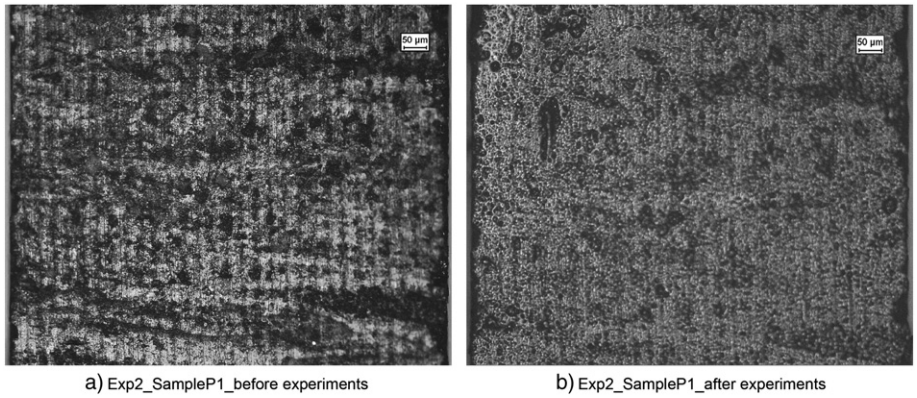

Fig. 7. Optical micrographs of Sample P1 taken before and after Exp2. Note that other than the difference in illumination conditions, the surface structure of the sample is unchanged after Exp2 compared with beforehand. No evidence of microcracking or other damage was found at the scale of observation used.

In the following, we discuss the mechanisms responsible for the observed anisotropy and hysteresis, and we attempt to explain the effects of sample size and relative humidity on swelling kinetics and equilibrium swelling strain. We also compare the swelling response of coal exposed to water vapour with the swelling caused by adsorption of other gases, such as CH_4, CO_2. In an attempt to gain insight into the single versus multilayer mechanism of water adsorption and the associated swelling response, we go on to compare our results on equilibrium swelling strain versus RH with presently available sorption/swelling models. Finally, we consider the possible implications of our findings for (E)CBM production.

4.1. Anisotropic swelling and hysteresis

4.1.1. Cause of anisotropic swelling behaviour

The results shown in Figs. 4 and 5 demonstrate that the swelling strains measured perpendicular to the bedding plane of our coal samples (i.e. in the *z* direction) tended to be larger than that parallel to bedding (in the *x* and *y* directions - refer Fig. 1), especially in the 1 mm samples and at RH values above 12–32%. The magnitude of this anisotropy, defined (following Day et al., 2010; Fry et al., 2009; Hol and Spiers, 2012; Pan and Connell, 2011) as the ratio of (apparent) equilibrium swelling strain in the *z* direction (e_z^{eq}) to the average value in the bedding plane, i.e. the average of e_x^{eq} and e_y^{eq}, is plotted versus relative humidity for all experimental runs in Fig. 8. During upward stepping of RH, the swelling anisotropy ratio for all experimental runs generally increased with increasing RH from 0.90 to 1.25 (mean 1.08), at 12% RH, to 1.10 to 1.45 (mean 1.24) at ~95% relative humidity. Taking into account swelling anisotropy ratios for all RH steps during upward stepping RH, we obtained an overall average anisotropy ratio of 1.13. A similar average trend was also observed during downward stepping RH but with clear differences due to effects of swelling hysteresis and departures from recoverability. Within these trends, our results (Fig. 8) show considerable variability not only amongst the samples, but also for individual samples depending on exposure history, i.e. from run to run on the same sample. In particular, the anisotropy ratios for the 4 mm sample (Exp4_SampleP3), and for the first run on 1 mm Sample P1, are consistently lower than for the other runs performed on 1 mm samples. Besides the anisotropic swelling described above, differences are observed between the strains e_x and e_y measured in the bedding plane (see Table 3). These differences might indicate that anisotropic swelling also occurred in bedding plane, so that e_x and e_y do not represent the principal strains.

Similar, anisotropic swelling behaviour of coal due to adsorption of water vapour was reported by Fry et al. (2009). These authors found similar maximum volumetric swelling strain magnitudes (1.32–1.74% at 97% RH) to ours for high volatile bituminous coal, and similar anisotropy ratios (on average around 1.2) to ours for coals ranking from subbituminous to bituminous and for all relative humidity steps employed in their experiments. However, the anisotropy ratios were found to vary remarkably amongst the samples. Fry et al. argued that, besides measurement errors, the observed variability might be related to the inhomogeneity of the samples, with different macerals responding differently to moisture sorption. However, they did not propose any explanation for the cause of the swelling anisotropy. Here, we propose that the swelling anisotropy of coal matrix material is caused either by a) anisotropic elastic properties due to the layered structure of coal matrix material, or b) anisotropic/layered sorption. These hypotheses are tested in the following, by comparison of our data with literature findings for adsorption of gases, such as CO_2 and CH_4.

Swelling anisotropy effects in coal, due to adsorption of gases, such as CO_2, CH_4 and N_2, have been widely reported by other workers (e.g. Day et al., 2010; Hol and Spiers, 2012; Pan and Connell, 2011). Pan and Connell (2011) proposed that swelling anisotropy is caused by anisotropy in the coal's elastic properties which is in turn determined by its layered/bedded matrix structure. Their argument was supported by good agreement between a model that assumes an anisotropic, linear elastic swelling response to isotropic internal stressing, caused by isotropic sorption, with swelling data for an unconfined Australian bituminous coal. Pan and Connell's explanation is also supported by a similar model developed by Espinoza et al. (2013), which successfully explained the experimental data reported by Hol and Spiers (2012) on anisotropic swelling of unconfined high volatile bituminous coal matrix samples exposed to CO_2 (Brzeszcze coal cylinders 4 mm in diameter, by 4 mm in length).

However, the anisotropic elastic swelling models proposed by Pan and Connell (2011) and by Espinoza et al. (2013) cannot explain all of our findings, notably that swelling anisotropy is related to relative humidity and exposure history (Fig. 8). This is because elastically controlled swelling anisotropy (linear elastic constants) should be independent of relative humidity value and of exposure history. Our experiments showed considerable effects, and considerable variability in effects, of RH and exposure history on swelling anisotropy. Therefore while part of the anisotropic swelling/shrinkage behaviour seen in our samples is likely due to linear elastic anisotropy of the samples, other factors must play a role too. Possibilities include a) an anisotropic distribution of micro-fractures present in the coal matrix, imparting anisotropic, non-linear elastic swelling behaviour or anisotropic water vapour access (Hol et al., 2014), b) a preferred orientation distribution (layering) of adsorption sites (i.e. oxygen functional groups) (Pan and

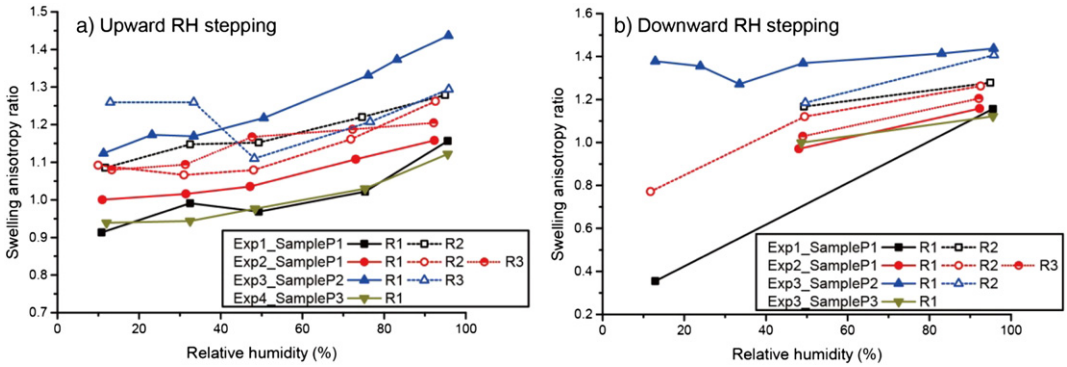

Fig. 8. Swelling anisotropy ratio $e_z^{eq}/(\frac{e_x^{eq}+e_y^{eq}}{2})$ versus RH data plotted for the present coal sample. Note that e_z^{eq} is the swelling strain measured perpendicular to bedding, whereas the swelling strain of the coal matrix samples parallel to bedding is taken as the average of e_x^{eq} and e_y^{eq}. a) Data obtained during upward stepping of RH. b) Data obtained during downward stepping of RH.

Connell, 2011) or c) multiple layer adsorption of water molecules or molecular clusters in layers parallel to bedding. To distinguish between the above possible explanations, further studies are needed.

4.1.2. Recoverability of swelling strain

The swelling/shrinkage versus RH data presented in Figs. 5 and 6 show closely recoverable behaviour (i.e. recovery of starting sample dimensions) after almost all experimental runs. An exception is Exp_SampleP1_R1, which showed excess shrinkage after RH cycling. In most cases, though, no permanent expansion or contraction occurred during adsorption-desorption. Similar recoverable swelling of coal upon water vapour sorption was also reported by Fry et al. (2009). This behaviour is consistent with swelling being caused by reversible adsorption of water (see also Pan, 2012). On this basis, we infer that permanent coal softening or plasticisation effects (c.f. Immergut and Mark, 1965) play little or no role in determining the swelling behaviour of coal during exposure to water vapour (as inferred for CO_2 sorption by Hol et al., 2012b). In Exp1_SampleP1_R1 (Fig. 5a), the 0.08% excess shrinkage observed in the z direction after RH cycling might result from residual moisture trapped in the sample prior to performing the experiments (Hol et al., 2012b), despite the fact that the sample was dried for one week under vacuum and was then exposed to 0.1% relative humidity at the start of Exp1. This explanation is supported by the evidence that the maximum swelling strains measured at RH = 95% in Exp1_SampleP1_R1, if added to the final excess shrinkage, take values of $e_z^{eq} = 0.55\%$, $e_y^{eq} = 0.4\%$, $e_x^{eq} = 0.44\%$, which are closely similar to the maximum e_i^{eq} values measured in Exp1_R2 and Exp2 performed on Sample P1. The implication for Sample P1 is that trapped moisture present before Run1 may have been removed through new transport paths created in the coal matrix during Run1, via the development of microfractures caused by heterogeneous swelling, e.g. on the maceral scale (see also Espinoza et al., 2015; Hol et al., 2012b, 2014).

4.1.3. Swelling hysteresis

Swelling/shrinkage hysteresis was observed in almost all of our experiments (see Figs. 5 and 6). The origin of this hysteresis cannot be directly determined from the current experimental results. However, the following possible causes of swelling hysteresis have been proposed in the literature on coal. These are now discussed in comparison with our experimental observations.

1) Sorption hysteresis. This refers to hysteresis observed in isothermal, water adsorption-desorption experiments performed on coal, i.e. to hysteresis in adsorbed water concentration versus RH data (Charrière and Behra, 2010; McCutcheon et al., 2001, 2003). As swelling of coal is caused by sorption of water vapour (Fry et al., 2009; Pan, 2012), true sorption hysteresis must result in swelling hysteresis. However, the mechanisms responsible for water sorption hysteresis remain unresolved in previous studies. McCutcheon et al. (2003) attributed sorption hysteresis, observed in low rank coal (Carbon content <84.3%) at relative humidities >45%, to a capillary condensation-evaporation effect. This effect leads to differences in the relative pressure of filling versus emptying small pores, and was also argued by Lin (2010) to be the cause of hysteresis in the sorption behaviour of mesoporous solids in general (i.e. solids containing pores within 2–50 nm). This explanation for sorption hysteresis is consistent with the hysteresis effects seen in our experiments, and with our finding that equilibration times for swelling upon adsorption were different from those for shrinkage upon desorption. Capillary condensation may therefore have played a role in our experiments. However, the capillary condensation-evaporation effect cannot explain sorption hysteresis observed in high rank coal or in low rank coal at relative humidities <45% (Allardice and Evans, 1971; Evans, 1973; McCutcheon et al., 2003). Under these conditions, sorption hysteresis is generally attributed to effects of swelling hysteresis, i.e. to the effect of swelling on changes in pore structure of coal (e.g. Charrière and Behra, 2010; Mahajan and Walker, 1971; McCutcheon et al., 2003). On the basis of our data, and in the context of our experiments, we see no way to distinguish between cause and effect.
2) Heterogeneous swelling of coal upon water sorption. Hol et al. (2012b) reported hysteresis in the swelling behaviour of high volatile bituminous coal samples (4 mm cylinder) exposed to CO_2 at pressures up to 100 MPa and at 40 °C. However, the hysteresis disappeared after one or two CO_2 pressure cycles. Based on SEM observations, Hol et al. argued that the hysteresis was caused by development of micro-fractures in the first CO_2 pressure cycle, due to heterogeneous swelling at the maceral scale. This explanation is consistent with the observation by Hol et al. that the equilibration was much faster in CO_2 cycles beyond the first. However, heterogeneous swelling and associated microcracking do not explain the swelling hysteresis observed in the present experiments, because a) no change in apparent equilibration time was observed between our first and second relative humidity runs, and b) the observed swelling hysteresis did not disappear after the first cycle of exposure to water vapour.
3) Other possibilities. We note that the different extents of hysteresis visible in Fig. 6 might also reflect a) sampling effects related to the relatively few data obtained on shrinkage upon desorption of water vapour, b) incomplete equilibration following individual RH steps, or c) errors caused by correcting for RH effects on the dilatometer sensor signals.

Clearly, to understand the cause of swelling hysteresis in the coal matrix material investigated here, more swelling/shrinkage and corresponding sorption/desorption data are needed.

4.2. Effects of sample size on equilibration rate and equilibrium swelling strain

It is clear from the swelling strain versus time curves presented in Fig. 4 that the rate at which (apparent) equilibrium was approached was much faster in our experiments on 1 mm samples (Exp1–3, Samples P1, P2) than on the 4 mm sample (Exp4, Sample P3). To illustrate this further, we use the standard graphical method applied in the literature to analyze sorption/swelling kinetics (c.f. Busch and Gensterblum, 2011; Li et al., 2010; Staib et al., 2013, 2014). For a given sample, this method involves plotting the change in normalized volumetric swelling strain ($\Delta e_v(t)/\Delta e_v^{eq}$) versus time ($t$) elapsed after imposing a specific step in gas/vapour pressure or activity (in our case RH). In this ratio, $\Delta e_v(t)$ is the evolving change in volumetric strain per step, and Δe_v^{eq} is the change in equilibrium strain value resulting from each step. Representative plots of this ratio ($\Delta e_v(t)/\Delta e_v^{eq}$) versus time are presented in Fig. 9 for samples P1, P2, and P3, for the relative humidity step from ~75% to 95%. This figure confirms that the swelling rates for 1 mm samples (P1 and P2) are similar, and that the swelling rate of sample P3 (4 mm) is much slower following a given change in relative humidity. On this basis, we infer that the swelling kinetics of our samples during exposure to water vapour are indeed strongly influenced by sample size. It follows from this length scale dependence that the rate of time-dependent swelling of coal matrix during exposure to water vapour must be controlled by diffusion of water molecules through the nanoporous coal matrix, and not by the kinetics of the sorption reaction between water vapour molecules and their specific adsorption sites in the coal.

At the same time, our results in Fig. 6e clearly demonstrate that the volumetric swelling strain attained at equilibrium, at any given relative humidity, is similar for samples P1 and P2 (1 mm) and for P3 (4 mm). This implies that the equilibrium swelling strain of coal exposed to water vapour is insensitive to sample size, at least for the cleat-free coal matrix material. Moreover, our results show that the equilibrium volumetric strains of 1.37–1.43% attained in our Brzeszcze high volatile

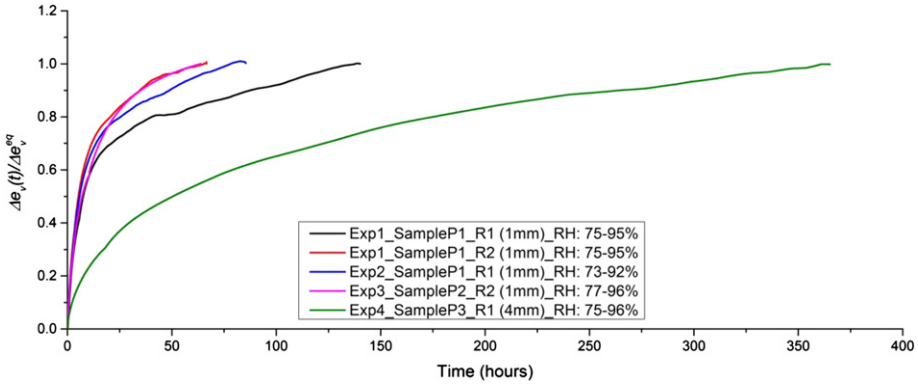

Fig. 9. Normalized volumetric swelling strain of samples P1, P2 and P3, (expressed as the ratio $\Delta e_v(t)/\Delta e_v^{eq}$) versus elapsed time following a step increase in relative humidity from ~75 to 95%. The quantity $\Delta e_v(t)$ represents the time-dependent change in volumetric swelling strain following the imposed step in RH (corrected for transient effects of RH on dilatometer sensor signals). The quantity Δe_v^{eq} represents the change in near equilibrium volumetric swelling strain produced by the RH step.

bituminous coal samples, when equilibrated with water vapour at 95% relative humidity at 40 °C, are similar to those reported in the literature for different coals and different sample sizes (Fry et al., 2009; Pan, 2012; van Bergen et al., 2009). Specifically, Fry et al. (2009) measured (apparent) equilibrium volumetric strains in the range of 1.32–1.74% for seven different high volatile bituminous coals, using $30 \times 9 \times 9$ mm^3 cylindrical samples tested at room temperature at 97% relative humidity. We infer that the effects of sample size and the presents of cleats on equilibrium swelling strain are probably small provided sufficient time is allowed for true equilibrium. On the other hand, our swelling kinetics analysis (Fig. 9) demonstrates that it might be impossible to reach true equilibration in experiments on coal samples beyond several cm in size, at least on practical lab time scales. Failure to reach equilibrium swelling in some experiments might even be due to sorption-induced swelling at fracture walls, causing fracture closure and reducing sample permeability even under unconfined conditions allowing free-expansion. A similar notion was recently put forward by Peng et al. (2014), who developed a conceptual model for permeability changes in coal due to diffusion and adsorption of gases.

4.3. Relationship between equilibrium swelling strain and RH: comparison with theory

4.3.1. Models for volumetric swelling strains versus activity of water vapour

The present results demonstrate a direct dependence of swelling strain at (apparent/near) equilibrium upon RH (see Figs. 4–6). Now we consider the relationship between adsorption-induced volumetric swelling strain (e_v^{eq}), adsorbed water concentration (C), and relative humidity (RH) or water vapour activity (a_g) from a theoretical perspective. We first consider the relationship between swelling strain e_v^{ads} and adsorbed water concentration C. It has been shown experimentally that, for coal ranking from lignite to bituminous, the swelling strain produced by water vapour sorption is linearly proportional to the adsorbed concentration C (mmol/g$_{coal}$) (Fry et al., 2009; Suuberg et al., 1993). On this basis, and noting the similar relation obtained by Hol and Spiers (2012) for swelling of unconfined coal matrix due to adsorption of CO_2, the equilibrium volumetric swelling strain caused by adsorption of water vapour can be expressed as

$$e_v^{eq} = C\rho V_0 \tag{1}$$

Here ρ represents the density (m^3/kg) of the coal matrix material, and V_0 (m^3/mol) represents the bulk volume change of the coal matrix due to adsorption of one mole of water molecules. V_0 can thus be viewed as the partial molar volume of adsorbed water molecules. The magnitude of V_0 for water molecules will in general depend on sorption bond strength and the response of the coal matrix to accommodating adsorbed molecules. V_0 accordingly depends on coal rank. Generally speaking, the higher the coal rank, the lower the measured magnitude of V_0. Fry et al. (2009) systematically measured the expansion and sorption response of 14 different bituminous coals and 1 sub-bituminous coal, to exposure to water vapour at relative humidities up to 97% at room temperature (22 °C). The results showed a linear relationship resembling Eq. (1) between the volumetric swelling strain and adsorbed concentration of water, yielding $V_0 = 4.3 \times 10^{-6}$ m^3/mol. From drying/shrinkage experiments on coals ranging from lignite to bituminous, Suuberg et al. (1993) obtained $V_0 = 12.9 \times 10^{-6}$ m^3/mol. In the present study on high volatile bituminous coal, we assume a value of V_0 based on the data of Fry et al. (2009), i.e. we assume $V_0 = 4.3 \times 10^{-6}$ m^3/mol.

Now we focus on the relation between adsorbed water concentration and water vapour activity. Direct measurement by FTIR (Mu and Malhotra, 1991) and ionic thermal current methods (Suárez et al., 1993) confirmed that adsorption of water vapour is strongly related to oxygen-bearing functional groups. Water molecules are therefore generally considered to be trapped primarily by oxygen-bearing functional groups present in the coal matrix, via hydrogen bonds (Allardice and Evans, 1971; Kaji et al., 1986; Mahajan and Walker, 1971; McCutcheon et al., 2003). Water thus adsorbed forms the first layer of adsorbed molecules, having high biding energy (c.f. Dubinin, 1980; Dubinin and Serpinsky, 1981). These adsorbed water molecules then form the secondary sites for attachment of additional water molecules with lower binding energy (c.f. Charrière and Behra, 2010; Lynch and Webster, 1982; McCutcheon et al., 2003; Nishino, 2001; Švábová et al., 2011). This multiple layer sorption mechanism is supported by experimental data on the concentration of adsorbed water molecules versus relative pressure obtained from isothermal sorption experiments performed on different rank coals (c.f. Charrière and Behra, 2010; McCutcheon et al., 2003; Švábová et al., 2011). The Brunauer-Emmett-Teller (BET) model, developed for multilayer sorption on the basis of Langmuir model (Brunauer et al., 1938), is the best-known and most commonly used model to describe water sorption (Charrière and Behra, 2010). It reduces to the Langmuir model if only single layer adsorption occurs. However, the BET model only fits water sorption data obtained at low relative humidity (Charrière and Behra, 2010; Skaar, 2012). Dent (1977) accordingly modified the BET model, assuming that the thermodynamic properties of water molecules adsorbed primarily by coal are different from those adsorbed secondarily. Writing the relative pressure of water vapour in terms of the activity of water vapour, the Dent model can be expressed as

$$C_1 = \frac{C_s K_1 a_g}{1 - K_2 a_g + K_1 a_g} \tag{2a}$$

$$C_2 = \frac{C_s K_1 K_2 a_g^2}{(1-K_2 a_g)(1-K_2 a_g + K_1 a_g)} \quad (2b)$$

where C_1 (mol/kg$_{coal}$) and C_2 (mol/kg$_{coal}$) represent the concentration of water molecules associated with primary adsorption and secondary adsorption, respectively. The quantity C_s (mol/kg$_{coal}$) represents the total number of localized adsorption sites (in mol) present in one kilogram of coal matrix for water molecules, while K_1 and K_2 represent the equilibrium constants for primary adsorption and secondary adsorption. Like the BET model, the Dent model assumes that the adsorption sites present in coal are available for both monolayer adsorption and multiple-layer adsorption. If no secondary adsorption occurs, the Dent model reduces to the single layer Langmuir model expressed in terms of gas activity as

$$C_1 = \frac{C_s K_1 a_g}{1 + K_1 a_g} \quad (3)$$

which is identical also to the single layer, localized sorption site model developed by Hol et al. (2012a) and by Liu et al. (submitted).

By contrast to the BET, Dent and Langmuir models, D'Arcy and Watt (1970) assumed that different functional groups present in the coal matrix are characterized by different adsorption mechanisms. They assumed that some adsorption sites allow monolayer adsorption with strong binding energy, some adsorption sites allow monolayer adsorption with weak binding energy, and some allow multiple layer adsorption. Neglecting the monolayer adsorption with weak binding energy, the D'Arcy and Watt (DW) model (Barton et al., 1994; Furmaniak et al., 2008; McCutcheon et al., 2003; Švábová et al., 2011) was formulated as a combination of the Langmuir isotherm for monolayer adsorption with strong binding energy (Langmuir, 1918), and the Dubinin and Serpinsky (DS1) isotherm (Dubinin and Serpinsky, 1981) for multiple-layer adsorption. Upon replacing the relative pressure of water vapour by the activity of water vapour, the result can be expressed as

$$C = \frac{C_{s1} K_1 a_g}{1 + K_1 a_g} + \frac{C_{s2} K_2 a_g}{1 - K_2 a_g} \quad (4)$$

Here C (mol/kg$_{coal}$) represents the total concentration of water molecules adsorbed, while C_{s1} and C_{s2} (mol/kg$_{coal}$) represent the number of localized adsorption sites (in mol) present in one kilogram of coal matrix for monolayer adsorption and for multiple-layer adsorption, respectively. The quantities K_1 and K_2 represent the equilibrium constants for monolayer adsorption and multiple-layer adsorption. In the DW model, monolayer adsorption is again identified as primary adsorption, while further multiple-layer adsorption is identified as secondary adsorption (McCutcheon et al., 2003; Švábová et al., 2011). If only single layer adsorption occurs, the model again reduces to the Langmuir type equation (c.f. Eq. (3)).

Having established relations between e_v^{eq} and C, and between C and a_g, we now consider the relation between e_v^{eq} and a_g, by combining Eqs. (1)–(4). We start from an end-member case that the swelling of coal upon water adsorption is caused solely by adsorption of a first layer of water molecules, as expressed via the Dent model (Eq. (3)), or solely by monolayer adsorption with strong biding energy as described via the DW model (Eq. (4)). Using Eq. (1), this end-member case can thus be formulated as

$$e_v^{eq} = \frac{C_s K a_g}{1 + K a_g} \rho V_0 \quad (5)$$

which is identical to the model developed by Hol and Spiers (2012) for swelling of unconfined coal matrix caused by adsorption of CO_2. For simplicity, we refer to this end-member case (i.e. Eq. (5)) as the HS swelling model. For the more general case, where the swelling is caused by both primary and secondary adsorption, we assume that V_0 is the same for all adsorbed water molecules, regardless of adsorption site type. Using the Dent and DW models, we accordingly obtain the following expressions for the total swelling of coal matrix material due to adsorption of water vapour, namely

$$e_v^{eq} = \rho V_0 (C_1 + C_2) = \rho V_0 C_s \left(\frac{K_1 a_g}{1 - K_2 a_g + K_1 a_g} + \frac{K_1 K_2 a_g^2}{(1-K_2 a_g)(1-K_2 a_g + K_1 a_g)} \right) \quad (6)$$

for the Dent-based case, and

$$e_v^{eq} = \rho V_0 \left(\frac{C_{s1} K_1 a_g}{1 + K_1 a_g} + \frac{C_{s2} K_2 a_g}{1 - K_2 a_g} \right) \quad (7)$$

for the DW-based case. Henceforth, we refer to Eqs. (6) and (7) as the Dent-based swelling model and the DW-based swelling model.

4.3.2. Swelling models versus experimental data

To compare our experimental data with the above models, we first convert our equilibrium volumetric swelling strain (e_v^{eq}) versus RH data (Fig. 6e) into e_v^{eq} versus water activity data. To do this, the activity (a_g) of water vapour at the experimentally imposed RH values was calculated using the EoS for water developed by Wagner and Pruß (2002). The results obtained for the upward RH steps of all experimental runs are plotted in Fig. 10 (omitting the data obtained for Exp1_SampleP1_R1, and that obtained for Exp4_SampleP3_R1 at an RH value of 12%, which have been shown above to be influenced by excess shrinkage and non-equilibrium swelling effects). Best fits of the HS, the Dent-based and the DW-based swelling models to the data plotted in Fig. 10 were obtained by means of non-linear regression, using $V_0 = 4.3 \times 10^{-6}$ m^3/mol (see Fig. 10). It is clearly seen that all three models fit the experimental data equally well. The HS model showed a near-linear fit, while the Dent-based and the DW-based models showed almost identical sigmoidal fits. The corresponding fitting parameter values are presented in Table 4, and all are reasonable when compared with those obtained from fits to previous sorption versus relative pressure data (c.f. Charrière and Behra, 2010; McCutcheon et al., 2003; Pan, 2012; Švábová et al., 2011). This means that the present study cannot distinguish between the three swelling models. For further progress, then, a better understanding of the mechanism

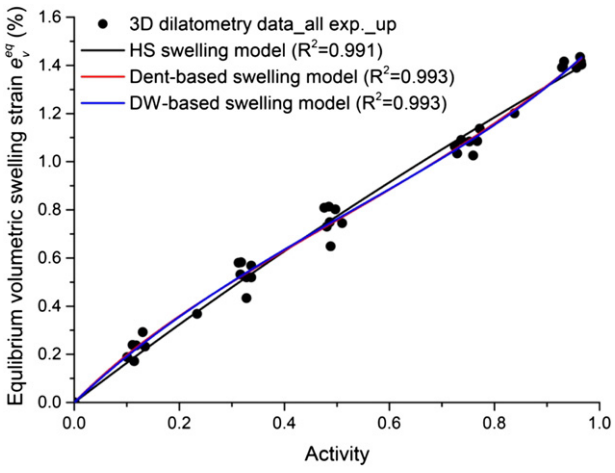

Fig. 10. Volumetric swelling strain at equilibrium versus water vapour activity. The black dots represent the experimental data obtained from the RH up-stepping portions of all experimental reported in Fig. 6e, except for Exp1_SampleP1_R1 and the data point attained at a RH value of 12% of Exp4_SampleP3_R1 (see text). The solid lines represent the best fits of the HS, the Dent-based and the DW-based models (Eqs. (5)–(7) respectively).

Table 4
Fitting parameter values of the models.

Model	C_s (mol/kg$_{coal}$)	K	C_{s1} (mol/kg$_{coal}$)	C_{s2} (mol/kg$_{coal}$)	K_1	K_2
HS	18.288	0.161				
Dent-based	1.671				2.346	0.480
DW-based			2.966	0.587	1.11	0.65

for swelling of coal matrix material due to adsorption of water vapour is needed.

4.4. Implications for ECBM

Our findings have a number of implications for (E)CBM production. These are considered pointwise below.

1. Our results demonstrate that the swelling of coal upon adsorption of water vapour increases with increasing relative humidity. This suggests that the use of water-free fluids for hydraulic fracturing of coal seams will produce better stimulation results than using aqueous fluids.
2. The present experiments have shown that the exposure of Brzeszcze high volatile bituminous coal to water vapour at 95% relative humidity at 40 °C, leads to adsorption-induced volumetric swelling strains of 1.37–1.43% at equilibrium. However, the same coal exhibits an equilibrium volumetric swelling strain of only 1.29–1.39% upon adsorption of CH_4 at a pressure of 10 MPa at 40 °C (Liu et al., submitted). Upon adsorption of CO_2 at the same *PT* conditions, equilibrium volumetric swelling strains of 2.37–2.47% are obtained (Hol and Spiers, 2012). Note that under in-situ conditions and especially in low rank coals, shrinkage effects upon drying might be even higher than that we measured, as a) the presence of bulk water can cause minor swelling in addition to sorption-induced swelling (Evans, 1973), and b) in our laboratory experiments, permanent shrinkage effects might have occurred upon the first drying event to affect our samples, e.g. after recovery from the Brzeszcze mine, during storage before experimentation, or possibly during the first drying step of each experiments (Busch and Gensterblum, 2011; Yu et al., 2013). This suggests that for high volatile bituminous coal, such as the Brzeszcze coal, reducing the in-situ water activity or relative humidity might shrink the coal, thus releasing methane, causing further shrinkage and hence creating self-enhancing transport paths (c.f. Fry et al., 2009; Levine, 1996; Liu et al., 2011; Moore, 2012). For other coal ranks under different in-situ conditions, the total shrinkage upon removing water and CH_4 will vary. However, an injection pressure of CO_2 can be designed at which the swelling strains caused by sorption of CO_2 can be counteracted.
3. On the basis of points 1 and 2, and taking into account that coal swelling strains caused by adsorption of N_2 are generally about half of that caused by CH_4 sorption at the same *PT* conditions (c.f. Battistutta et al., 2010; Day et al., 2010, 2012), it might be a good strategy to use (liquid) N_2 as a hydraulic-fracturing fluid to stimulate CBM production from coal seams. McDaniel et al. (1997) has shown that liquid N_2 injection is technically feasible. This could be followed by circulating dry gaseous N_2 to promote matrix shrinkage by removing water and methane, regardless of coal rank. After such a phase of N_2-ECBM production, i.e. after removing water and methane, CO_2 could be injected into the coal seam for geological storage. This strategy has two advantages. The first is that shrinkage upon removing water and CH_4 from coal seam will create more transport paths for CO_2 injection and storage. The second is that the larger swelling effect caused by adsorption of CO_2, compared with the shrinkage effect of removing water and CH_4 may result in self-sealing of coal seams.
4. Our experimental results demonstrate that the swelling/shrinkage response of coal matrix material to exposure to water vapour is rate controlled by diffusion. This means that diffusion of water between coal matrix material and cleat/fracture systems must be considered in predicting in-situ coal seam permeability evolution during (E)CBM production.

5. Conclusions

In this study, we have reported the results of detailed 3D eddy-current dilatometry experiments performed on two 1 mm and one 4 mm cubes of high volatile bituminous coal matrix material (Brzeszcze, Poland), exposed to water vapour. The experiments were conducted at relative humidities varied in the range 0.1 to 95%, under unconfined conditions and at a constant temperature of 40 °C. We considered the effects of sample size and relative humidity on swelling kinetics and on equilibrium swelling strain. The main findings and conclusions are summarized as follows:

1. The swelling response of our samples to water adsorption was anisotropic with the swelling strain developed perpendicular to bedding being on average about 1.13 times that occurring parallel to bedding on average, though this ratio varied with relative humidity. The swelling response was largely reversible and/or recoverable, with some hysteresis effects. The observed dependence of the swelling strain anisotropy ratio on RH suggests that the anisotropic swelling effect is not solely determined by elastic anisotropy of the coal studied.
2. Sample size was found to strongly influence the swelling kinetics of coal matrix material at a given relative humidity, but does not influence the magnitude of swelling strain attained at equilibrium. This confirms that time-dependent swelling/shrinkage of unconfined coal matrix during exposure to water vapour is controlled by diffusion of water molecules as opposed to sorption reaction kinetics.
3. The volumetric swelling strains attained by our coal samples at equilibrium showed a near-linear relation with relative humidity, reaching a value of 1.37–1.43% at around 95% relative humidity. This volumetric swelling strain, caused by exposure of Brzeszcze high volatile bituminous coal to water vapour at 95% relative humidity, is similar to that produced by exposure to and sorption of CH_4 at 10 MPa. By contrast, the observed volumetric swelling strain is about 0.6 times that caused by sorption of CO_2 at 10 MPa pressure.
4. Three models for swelling of unconfined coal matrix material due to water sorption have been developed. The three models respectively address the equilibrium swelling strain caused by mono-layer adsorption, by multiple-layer sorption, and by combined mono- plus multiple-layer adsorption. The equilibrium swelling strain versus RH or water activity data obtained in the present experiments can be well fitted by all three models, so that the mechanism dominating water vapour adsorption and associated swelling could not be pinpointed.
5. Our findings suggest that it might be a good strategy to use (liquid) N_2 as a hydraulic-fracturing fluid to stimulate the coal seams for CBM production, then circulating dry N_2 to promote the shrinkage due to removal of water and methane. CO_2 might later be injected into the coal seam for geological storage, resulting in self-sealing of fractures in the coal bed system due to the relatively large swelling strain caused by CO_2 sorption.

Acknowledgements

The China Scholarship Council (CSC) and Total S.A. are gratefully acknowledged for their financial support of first author Jinfeng Liu and of the research project.

Appendix A

A.1. The quality of RH control achieved using saturated salt solution buffers in the experiments reported in this paper is illustrated in Fig. A1 for a coal sample run. Note the rapid equilibration of RH throughout the system.

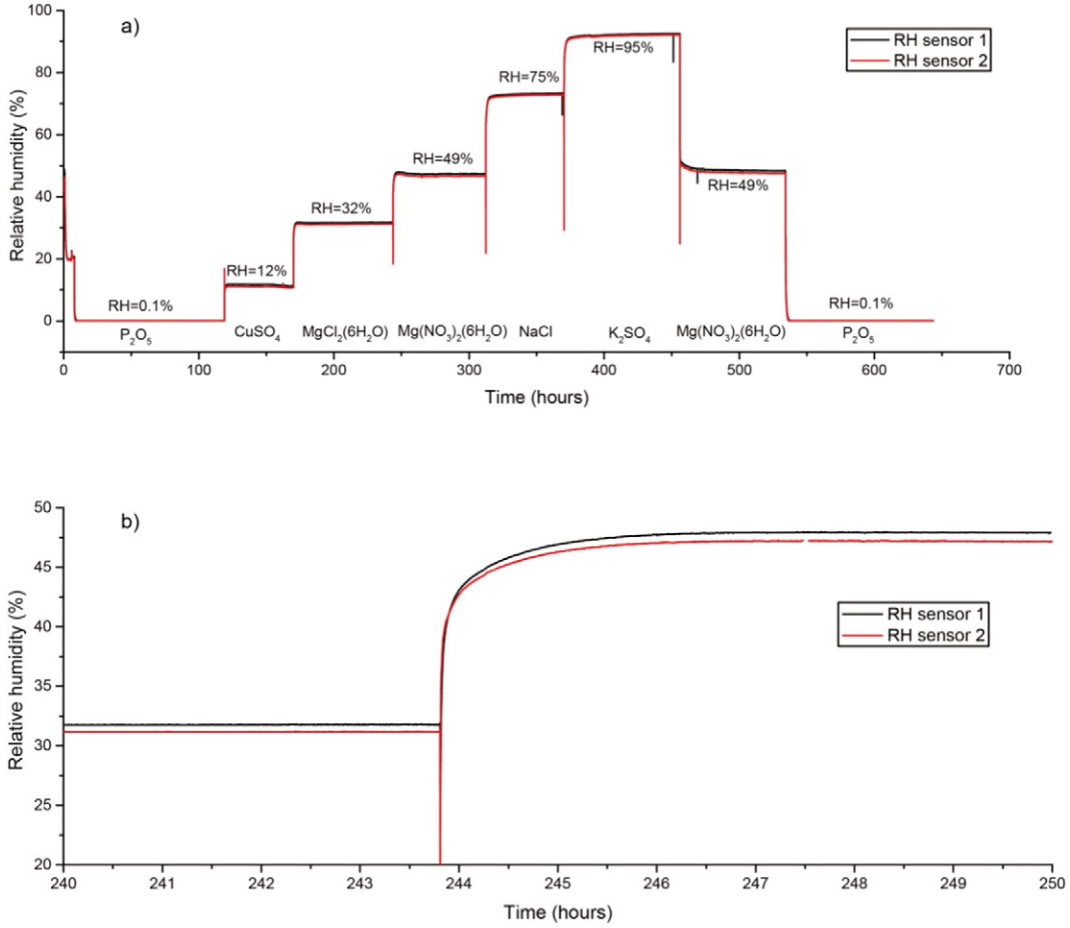

Fig. A1. Representative data showing relative humidity (%) measured by the digital relative humidity sensors as a function of time during our experiments. a) RH control achieved during a typical experiment using the salt buffer solutions indicated. b) Blow up of transient in RH upon change in RH from 32 ($MgCl_2 \cdot 6H2O$) to 49% ($Mg(NO_3)_2 \cdot 6H2O$).

A.2. The quality of temperature control achieved in the experiments is illustrated in Fig. A2.

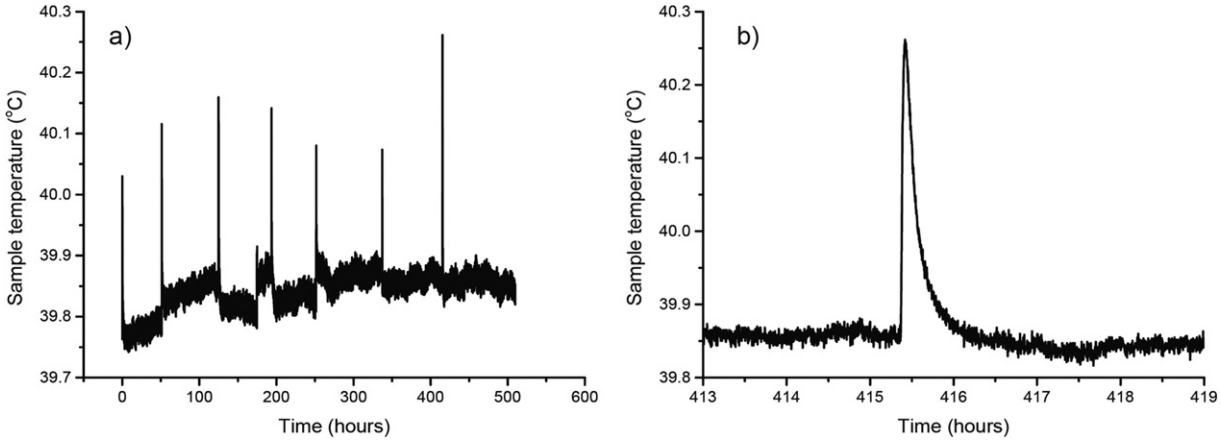

Fig. A2. Representative data showing the sample temperature measured using a PT-100 element versus time during a typical experiment. a) Aside from the spikes that occurred upon changing RH buffer, the sample temperature remained constant within ~0.1 °C. b) After an RH step (buffer change), stabilization of temperature took ~1 h.

A.3. Calibration of RH effect on sensor signals.

Since the 3D eddy current sensor is fully exposed to water vapour, sorption of water vapour on the sensor and by the electrical insulation covering the sensor cables (e.g. Pons et al., 2014) leads to time-dependent effects on the 3 orthogonal sensor signals. To determine the magnitude of these RH-related effects on sensor signals, control experiments were performed on three different dummy samples, namely one 4 mm stainless steel cube, one 1 mm stainless steel cube, and one 1 mm quartz glass cube, following identical experimental procedures as applied when using coal samples. After each relative humidity step, sensor signal changes slowly with time, typically reaching equilibrium in 1–2 days. The results confirm that the RH effects on sensor signals are insensitive to sample material and sample size. A typical curve for RH effects on sensor signals, expressed in terms of equivalent apparent swelling displacement, versus time, obtained from the control experiments, is plotted in Fig. 11. It is seen that the apparent swelling displacement versus time curve was similar in form to the uncorrected swelling/shrinkage of coal samples versus time.

In addition, the results shown in Fig. 11 demonstrate that the RH effects on sensor signals cannot be neglected. This means that to determine the true response of coal sample during exposure to water vapour, we must correct for this effect. Equilibrium effects of RH changes on sensor signals were corrected for using fitted functions describing near equilibrium sensor signals, expressed in terms of apparent displacement (μm), versus RH. For RH upward stepping, we applied the non-linear regression method to fit the hyperbolic function $y = \frac{ax}{1-bx}$ to the apparent displacement versus RH data for each sensor at or near equilibrium (see Fig. 12a). For RH downward steps, the apparent displacement data were fitted using linear regression (see Fig. 12b), because insufficient data points were obtained from the two relative humidity steps implemented to allow non-linear regression. The best fits (dashed lines) shown in Fig. 12 were used to describe the effect of RH on sensor signal and apparent equivalent swelling at equilibrium.

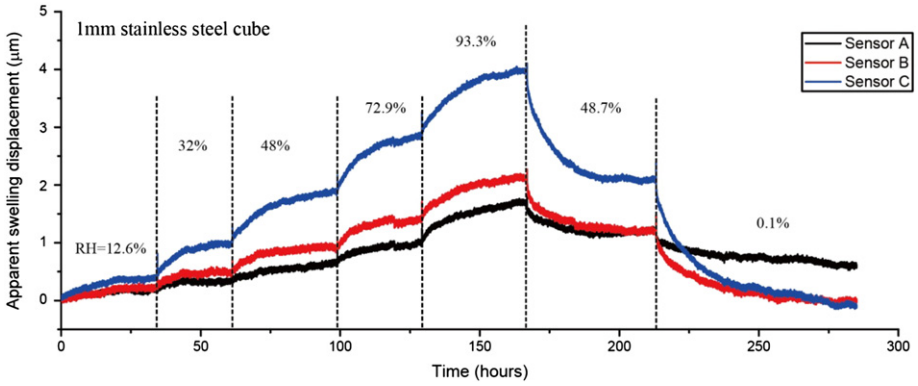

Fig. 11. Representative data showing RH effects on sensor signals, expressed in terms of equivalent apparent swelling displacement (μm) versus time.

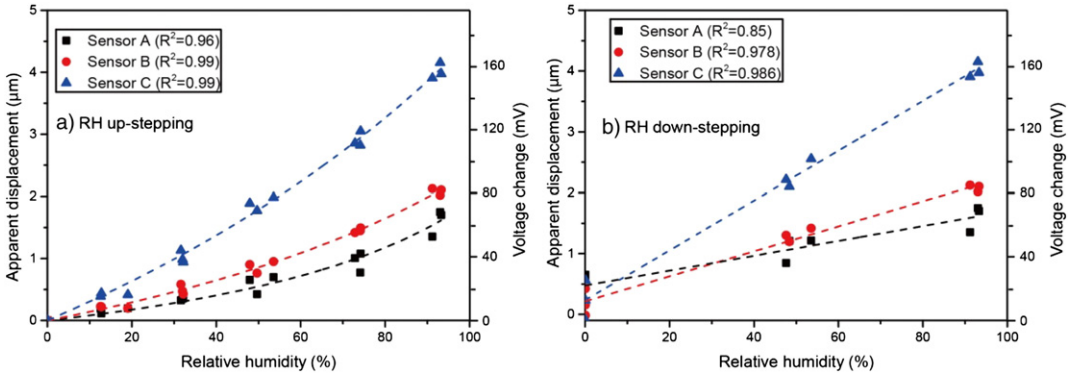

Fig. 12. Apparent displacement measured by each sensor in the 3D dilatometer at or near equilibrium for all dummy samples, plotted as a function of relative humidity. a) RH up-stepping sequence. The solid symbols represent the apparent target displacement by each sensor purely due to the effect of RH change on the sensor system. The dashed lines represent non-linear regression fits. b) RH down-stepping sequence. The solid symbols again represent apparent target displacement measured by each sensor, and the dashed lines represent the linear regression fits to the very limited data.

References

Allardice, D., Evans, D., 1971. The-brown coal/water system: part 2. Water sorption isotherms on bed-moist Yallourn brown coal. Fuel 50, 236–253.

Barton, S., Evans, M., MacDonald, J., 1994. Adsorption of water vapor on nonporous carbon. Langmuir 10, 4250–4252.

Battistutta, E., Van Hemert, P., Lutynski, M., Bruining, H., Wolf, K.-H., 2010. Swelling and sorption experiments on methane, nitrogen and carbon dioxide on dry Selar Cornish coal. Int. J. Coal Geol. 84, 39–48.

Brunauer, S., Emmett, P.H., Teller, E., 1938. Adsorption of gases in multimolecular layers. J. Am. Chem. Soc. 60, 309–319.

Busch, A., Gensterblum, Y., 2011. CBM and CO_2-ECBM related sorption processes in coal: a review. Int. J. Coal Geol. 87, 49–71.

Charrière, D., Behra, P., 2010. Water sorption on coals. J. Colloid Interface Sci. 344, 460–467.

D'Arcy, R., Watt, I., 1970. Analysis of sorption isotherms of non-homogeneous sorbents. Trans. Faraday Soc. 66, 1236–1245.

Day, S., Fry, R., Sakurovs, R., 2008a. Swelling of Australian coals in supercritical CO_2. Int. J. Coal Geol. 74, 41–52.

Day, S., Sakurovs, R., Weir, S., 2008b. Supercritical gas sorption on moist coals. Int. J. Coal Geol. 74, 203–214.

Day, S., Fry, R., Sakurovs, R., Weir, S., 2010. Swelling of coals by supercritical gases and its relationship to sorption. Energy Fuel 24, 2777–2783.

Day, S., Fry, R., Sakurovs, R., 2011. Swelling of moist coal in carbon dioxide and methane. Int. J. Coal Geol. 86, 197–203.
Day, S., Fry, R., Sakurovs, R., 2012. Swelling of coal in carbon dioxide, methane and their mixtures. Int. J. Coal Geol. 93, 40–48.
Dent, R., 1977. A multilayer theory for gas sorption part I: sorption of a single gas. Text. Res. J. 47, 145–152.
Dubinin, M., 1980. Water vapor adsorption and the microporous structures of carbonaceous adsorbents. Carbon 18, 355–364.
Dubinin, M., Serpinsky, V., 1981. Isotherm equation for water vapor adsorption by microporous carbonaceous adsorbents. Carbon 19, 402–403.
Espinoza, D., Vandamme, M., Dangla, P., Pereira, J.M., Vidal-Gilbert, S., 2013. A transverse isotropic model for microporous solids: application to coal matrix adsorption and swelling. J. Geophys. Res. Solid Earth 118, 6113–6123.
Espinoza, D., Pereira, J.-M., Vandamme, M., Dangla, P., Vidal-Gilbert, S., 2015. Desorption-induced shear failure of coal bed seams during gas depletion. Int. J. Coal Geol. 137, 142–151.
Evans, D.G., 1973. The brown-coal/water system: part 4. Shrinkage on drying. Fuel 52, 186–190.
Fry, R., Day, S., Sakurovs, R., 2009. Moisture-induced swelling of coal. Int. J. Coal Prep. Util. 29, 298–316.
Furmaniak, S., Gauden, P.A., Terzyk, A.P., Rychlicki, G., 2008. Water adsorption on carbons—critical review of the most popular analytical approaches. Adv. Colloid Interf. Sci. 137, 82–143.
Gensterblum, Y., Merkel, A., Busch, A., Krooss, B.M., 2013. High-pressure CH_4 and CO_2 sorption isotherms as a function of coal maturity and the influence of moisture. Int. J. Coal Geol. 118, 45–57.
Gensterblum, Y., Busch, A., Krooss, B.M., 2014. Molecular concept and experimental evidence of competitive adsorption of H_2O, CO_2 and CH_4 on organic material. Fuel 115, 581–588.
Hol, S., Spiers, C.J., 2012. Competition between adsorption-induced swelling and elastic compression of coal at CO_2 pressures up to 100 MPa. J. Mech. Phys. Solids.
Hol, S., Peach, C.J., Spiers, C.J., 2011. Applied stress reduces the CO_2 sorption capacity of coal. Int. J. Coal Geol. 85, 128–142.
Hol, S., Peach, C.J., Spiers, C.J., 2012a. Effect of 3-D stress state on adsorption of CO_2 by coal. Int. J. Coal Geol. 93, 1–15.
Hol, S., Spiers, C.J., Peach, C.J., 2012b. Microfracturing of coal due to interaction with CO_2 under unconfined conditions. Fuel 97, 569–584.
Hol, S., Gensterblum, Y., Massarotto, P., 2014. Sorption and changes in bulk modulus of coal—experimental evidence and governing mechanisms for CBM and ECBM applications. Int. J. Coal Geol. 128, 119–133.
Immergut, E.H., Mark, H.F., 1965. Principles of Plasticization.
Kaji, R., Muranaka, Y., Otsuka, K., Hishinuma, Y., 1986. Water absorption by coals: effects of pore structure and surface oxygen. Fuel 65, 288–291.
Langmuir, I., 1918. The adsorption of gases on plane surfaces of glass, mica and platinum. J. Am. Chem. Soc. 40, 1361–1403.
Levine, J.R., 1996. Model study of the influence of matrix shrinkage on absolute permeability of coal bed reservoirs. Geol. Soc. Lond., Spec. Publ. 109, 197–212.
Li, D., Liu, Q., Weniger, P., Gensterblum, Y., Busch, A., Krooss, B.M., 2010. High-pressure sorption isotherms and sorption kinetics of CH_4 and CO_2 on coals. Fuel 89, 569–580.
Lin, W., 2010. Gas Sorption and the Consequent Volumetric and Permeability Change of Coal.
Liu, J., Chen, Z., Elsworth, D., Qu, H., Chen, D., 2011. Interactions of multiple processes during CBM extraction: a critical review. Int. J. Coal Geol. 87, 175–189.
Lynch, L.J., Webster, D.S., 1982. Effect of thermal treatment on the interaction of brown coal and water: a nuclear magnetic resonance study. Fuel 61, 271–275.
Mahajan, O., Walker, P., 1971. Water adsorption on coals. Fuel 50, 308–317.
McCutcheon, A., Barton, W., Wilson, M., 2001. Kinetics of water adsorption/desorption on bituminous coals. Energy Fuel 15, 1387–1395.
McCutcheon, A.L., Barton, W.A., Wilson, M.A., 2003. Characterization of water adsorbed on bituminous coals. Energy Fuel 17, 107–112.
McDaniel, B., Grundmann, S.R., Kendrick, W.D., Wilson, D.R., Jordan, S.W., 1997. Field applications of cryogenic nitrogen as a hydraulic fracturing fluid. SPE Annual Technical Conference and Exhibition. Society of Petroleum Engineers.
Merkel, A., Gensterblum, Y., Krooss, B.M., Amann, A., 2015. Competitive sorption of CH_4, CO_2 and H_2O on natural coals of different rank. Int. J. Coal Geol. 150, 181–192.
Moore, T.A., 2012. Coalbed methane: a review. Int. J. Coal Geol. 101, 36–81.
Mu, R., Malhotra, V., 1991. A new approach to elucidate coal-water interactions by an in situ transmission FT-ir technique. Fuel 70, 1233–1235.
Nishino, J., 2001. Adsorption of water vapor and carbon dioxide at carboxylic functional groups on the surface of coal. Fuel 80, 757–764.
Pan, Z., 2012. Modeling of coal swelling induced by water vapor adsorption. Front. Chem. Sci. Eng. 6, 94–103.
Pan, Z., Connell, L.D., 2011. Modelling of anisotropic coal swelling and its impact on permeability behaviour for primary and enhanced coalbed methane recovery. Int. J. Coal Geol. 85, 257–267.
Pan, Z., Wood, D.A., 2015. Coalbed methane (CBM) exploration, reservoir characterisation, production, and modelling: a collection of published research (2009–2015). J. Nat. Gas Sci. Eng. 26, 1472–1484.
Pan, Z., Connell, L.D., Camilleri, M., Connelly, L., 2010. Effects of matrix moisture on gas diffusion and flow in coal. Fuel 89, 3207–3217.
Peng, Y., Liu, J., Wei, M., Pan, Z., Connell, L.D., 2014. Why coal permeability changes under free swellings: new insights. Int. J. Coal Geol. 133, 35–46.
Pons, E., Yrieix, B., Heymans, L., Dubelley, F., Planes, E., 2014. Permeation of water vapor through high performance laminates for VIPs and physical characterization of sorption and diffusion phenomena. Energy Build. 85, 604–616.
Skaar, C., 2012. Wood-Water Relations. Springer Science & Business Media.
Staib, G., Sakurovs, R., Gray, E.M.A., 2013. A pressure and concentration dependence of CO_2 diffusion in two Australian bituminous coals. Int. J. Coal Geol. 116, 106–116.
Staib, G., Sakurovs, R., Gray, E.M., 2014. Kinetics of coal swelling in gases: Influence of gas pressure, gas type and coal type. Int. J. Coal Geol. 132, 117–122.
Suárez, N., Laredo, E., Nava, R., 1993. Characterization of four hydrophilic sites in bituminous coal by ionic thermal current measurements. Fuel 72, 13–18.
Suuberg, E.M., Otake, Y., Yun, Y., Deevi, S.C., 1993. Role of moisture in coal structure and the effects of drying upon the accessibility of coal structure. Energy Fuel 7, 384–392.
Švábová, M., Weishauptová, Z., Přibyl, O., 2011. Water vapour adsorption on coal. Fuel 90, 1892–1899.
van Bergen, F., Pagnier, H., Krzystolik, P., 2006. Field experiment of enhanced coalbed methane-CO_2 in the upper Silesian basin of Poland. Environ. Geosci. 13, 201–224.
van Bergen, F., Spiers, C., Floor, G., Bots, P., 2009. Strain development in unconfined coals exposed to CO_2, CH_4 and Ar: effect of moisture. Int. J. Coal Geol. 77, 43–53.
Wagner, W., Pruß, A., 2002. The IAPWS formulation 1995 for the thermodynamic properties of ordinary water substance for general and scientific use. J. Phys. Chem. Ref. Data 31, 387–535.
White, C.M., Smith, D.H., Jones, K.L., Goodman, A.L., Jikich, S.A., LaCount, R.B., DuBose, S.B., Ozdemir, E., Morsi, B.I., Schroeder, K.T., 2005. Sequestration of carbon dioxide in coal with enhanced coalbed methane recovery a review. Energy Fuel 19, 659–724.
Yu, J., Tahmasebi, A., Han, Y., Yin, F., Li, X., 2013. A review on water in low rank coals: the existence, interaction with coal structure and effects on coal utilization. Fuel Process. Technol. 106, 9–20.